nks

Nordisk kernesikkerhedsforskning
Norrænar kjarnöryggisrannsóknir
Pohjoismainen ydinturvallisuustutkimus
Nordisk kjernesikkerhetsforskning
Nordisk kärnsäkerhetsforskning
Nordic nuclear safety research

NKS-112
ISBN 87-7893-173-8

Ex-Vessel Coolability and Energetics of Steam Explosions in Nordic Light Water Reactors EXCOOLSE Project Report 2004

H. S. Park, A. K. Nayak, R. C. Hansson & B. R. Sehgal
Royal Institute of Technology, Sweden

October 2005

Abstract

Beyond-the-design-basis accidents, i.e. severe accidents, involve melting of the nuclear reactor core and release of radioactivity. Intensive research has been performed for years to evaluate the consequence of the postulated severe accidents.
Severe accidents posed, to the reactor researchers, a most interesting and most difficult set of phenomena to understand, and to predict the consequences, for the various scenarios that could be contemplated. The complexity of the interactions, occurring at such high temperatures (~2500ºC), between different materials, which are changing phases and undergoing chemical reactions, is simply indescribable with the accuracy that one may desire. Thus, it is a wise approach to pursue research on SA phenomena until the remaining uncertainty in the predicted consequence, or the residual risk, can be tolerated.
In the PRE-DELI-MELT project (Sehgal and Park, 2004) at NKS, several critical issues on the core melt loadings in the BWR and PWR reactor containments were identified.
Many of Nordic nuclear power plants, particularly in boiling water reactors, adopted the Severe Accident Management Strategy (SAMS) which employed the deep subcooled water pool in lower dry-well. The success of this SAMS largely depends on the issues of steam explosions and formation of debris bed and its coolability.
From the suggestions of the PRE-DELI-MELT project, a series of research plan was proposed to investigate the remaining issues specifically on the ex-vessel coolability of corium during severe accidents;

(a) ex-vessel coolability of the melt or particulate debris, and
(b) energetics and debris characteristics of fuel-coolant interactions endangering the integrity of the reactor containments.

Key words

Severe accidents, melt coolability, ex-vessel, debris characteristics

NKS-112
ISBN 87-7893-173-8

Electronic report, October 2005

The report can be obtained from
NKS Secretariat
NKS-775
P.O. Box 49
DK - 4000 Roskilde, Denmark

Phone +45 4677 4045
Fax +45 4677 4046
www.nks.org
e-mail nks@nks.org

Ex-Vessel Coolability and Energetics of Steam Explosions in Nordic Light Water Reactors

EXCOOLSE Project Report 2004

H. S. Park, A. K. Nayak, R. C. Hansson, B. R. Sehgal

Royal Institute of Technology
Division of Nuclear Power Safety
Stockholm, Sweden

October 2005

Contents

Figures

Tables

Chapter 1
Introduction and Project Background

1.1 Introduction

1.1.1 Severe Accident Safety and Issues

The main safety goal of modern nuclear power plants is to ensure the public safety against radioactivity which may be released during reactor accidents. To achieve this goal the reactors have been designed with the defense-in-depth concept and built upon the design-based accidents (LOCA) which involves the loss of cooling due to the break of the main coolant pipelines. However, Three Mile Island 2 (TMI-2) accident (Broughton et al., 1989) deepened a public concern of the accident progression further beyond the design-based accidents which lead to core meltdown. These beyond-the-design-basis accidents, i.e., severe accidents, clearly involve melting of the nuclear reactor core and release of radioactivity. Intensive research has been performed for years to evaluate the consequence of the postulated severe accidents. It is clear that maintenance of the integrity of reactor vessel and containment is a key to ensure the public safety against risk resulted from severe accidents.

Severe accidents posed, to the reactor researchers, a most interesting and most difficult set of phenomena to understand, and to predict the consequences, for the various scenarios that could be contemplated. The complexity of the interactions, occurring at such high temperatures (~2500ºC), between different materials, which are changing phases and undergoing chemical reactions, is simply indescribable with the accuracy that one may desire. Thus, it is a wise approach to pursue research on SA phenomena until the remaining uncertainty in the predicted consequence, or the residual risk, can be tolerated.

In the PRE-DELI-MELT project (Sehgal and Park, 2004) at NKS, several critical issues on the core melt loadings in the BWR and PWR reactor containments were identified, and the comprehensive assessment of severe accident management schemes adopted currently in Nordic BWRs and PWRs was performed. Also the final report suggested the experimental research facilities in the Nordic countries which had potential to utilize to resolve the issues. The report emphasized that research efforts should focus on following severe accident management issues:

(a) Coolability of the melt pool or particulate debris.
(b) Energetics and debris characteristics of fuel-coolant interaction.
(c) Vessel failure.

Many of Nordic nuclear power plants, particularly in boiling water reactors, adopted the Severe Accident Management Strategy (SAMS) which employed the deep subcooled water pool in lower dry-well. The success of this SAMS largely depends on the issues of steam explosions and formation of debris bed and its coolability.

From the suggestions of the PRE-DELI-MELT project, a series of research plan was proposed to investigate the remaining issues specifically on the ex-vessel coolability of corium during severe accidents;

(a) ex-vessel coolability of the melt or particulate debris, and
(b) energetics and debris characteristics of fuel-coolant interactions endangering the integrity of the reactor containments.

1.1.2 Debris Bed Coolability

During a severe accident in a nuclear power plant, the core melt can fail the reactor vessel and relocate into the containment. In this situation, the ex-vessel retention could be realized by the direct debris cooling in the containment with the water of the existing reactor safety cooling system, the water of the additional safety measure in a core catcher, or the combination of both measures. In some Nordic accident management schemes the vessel cavity is flooded with water before the vessel failure, resulting in formation of a particulate debris bed on the cavity floor due to melt break-up in water. If no more water is available, the existing water will evaporate in time resulting in a dry particulate bed which is still generating decay heat. The hot bed which stands on a concrete base may start attacking the base of concrete. During the MCCI, non-condensable gases including water vapor are generated which flow upwards through the porous particulate bed.

The main parameters affecting the coolability of the debris bed are its porosity which is a function of the size and the shape of the particles which constitute the debris bed, the operating condition such as water entry from the top or the bottom of the debris bed, water temperature and the magnitude of non-condensable gas generated during MCCI. The debris bed can have a non-uniform particle distribution or porosity stratification. Tests conducted in the FARO series (Magallon *et al*., 1999) as well as in KROTOS (Huhtiniemi *et al.*, 1999) with prototypic material showed that the debris bed formed due to melt fragmentation in water, constitutes particles of various sizes ranging from close to 0 mm to slightly more than 6 mm. In the KROTOS tests, most of the particles were found to remain in the range of 0.045 to 2.0 mm. In the FARO tests (L-24 and L-31), the particles were found to be in the size between 0.7 mm and 6.0 mm. Similarly in the CCM tests conducted at the Argonne National Laboratory (Spencer *et al.*, 1994), most of the particles were found to lie between 0.25 and 10 mm. It is not only the size of the particles but also the porosity of the debris bed, which influence the coolability during the flooding.

Similar to the non-uniformity of the particle size distribution, the debris bed formed is found to have a non-uniform porosity distribution. The smaller size particles are carried by the steam to the boundaries during the melt fragmentation process and some of the unfragmented pieces as well as the large size particles stay at the centre of the bed. This process can form a radially stratified bed with lower porosity at the centre of the bed and higher porosity at the periphery. This can also happen not only in radial directions but also in axial directions. In the COTEL tests (Nagasaka *et al*., 1999) the debris bed formed with prototypic material was found to be like a sand bed. Most of the tests conducted so far have revealed that the porosity of the debris bed lie between 0.2 and 0.4. It is of interest to investigate the quenching behavior in stratified configurations when the bed is flooded and generating heat and compare it with that

of a uniform particulate bed. The additional interest is to find out the effects of non-condensable gases which can enhance the counter current flooding limitation (CCFL), on the quenching of bed.

Numerous experimental studies were conducted in small scale facilities in the early 80's to estimate coolability of particulate beds (Hardee and Nilson, 1977, Dhir and Catton, 1977, Catton *et al.,* 1983, Reed *et al.*, 1985). They found the effects of bed height, pressure, particle size distribution and porosity on the coolability of debris beds.

Cho and Bova (1983) found that during top flooding process, the quench front propagates faster in the middle of the bed than in the outer regions. Schrock *et al.* (1984) have studied the flooding of an isothermal particle bed with steam and water. Hu and Theofanous (1984) have investigated the coolability behavior of deep volumetrically heated particle beds. Tung and Dhir (1987) conducted experiments in debris beds with both radial and axial porosity distributions. They used steel particles for formation of the debris bed and heated the bed inductively. They found that the quench front velocity is controlled by the counter-current flooding limit during top flooding of an axially stratified layer. During top flooding of a radially stratified porous layer, they observed very little cross-flow at the boundary between the layers. The quenching was found to occur in the high porosity region while the low porosity region was found to get quenched by bottom flooding mode due to inflow of liquid from the quenched high porosity region. However, the size of particles they used in the tests, were relatively much larger than the actual debris size.

Tung et al. (1986) conducted coolability experiments with top flooding and gas injection and investigated the quenching behavior. Sehgal et al. (2001) studied the quenching characteristics of homogenous particle beds and axially stratified particle beds with top and bottom flooding using downcomers of different size. They found out that the quenching period is decided by the low porosity particles and their sizes. Also, the quenching period is found to be reduced significantly with bottom flooding. More recently, Jasiulevicius and Sehgal (2003) investigated the quenching behavior of homogenous particle beds with non-condensable gas addition from bottom. They found that the non-condensable gas affects the quenching period.

Several questions addressed in the previous paragraphs are not sufficiently answered yet to understand the coolability of particulate corium debris beds, such as;

(a) the effect of porosity and size of debris bed,
(b) the effect of debris bed configuration (debris bed stratification),
(c) the effect of various cooling passages (top, side and bottom) in the multi-dimensional configurations, etc.

1.1.3 Melt Pool Coolability

If the molten corium is relocated in the containment cavity and formed a melt pool, the most convenient accident management strategy is to cool the melt pool by flooding it from the top. However, the question that arises is to what extent the water ingress in the corium pool to quench and cool it.

From the MACE experimental program (Sehgal *et al.*, 1992, Merilo *et al.*, 1997), the characteristics of melt pool formation associated with quenching by water can be hinted. It was found that a tough crust is formed on the upper surface of the melt pool during top flooding situation, which was found to limit the access of the water overlayer to the melt pool below the crust. Posttest examination of the M3b debris of the MACE tests indicates that the crust thickness was about 10 cm, amounting to ½ of the initial mass (Farmer *et al.*, 2000). After 20 minutes of melt/water heat transfer in M3b, several independent sources of data indicate that the crust had anchored to the test section side walls and the melt separated from the crust (Farmer and Spencer, 2001). After separation, melt/water heat transfer rate dropped significantly, thereby terminating the initial quenching event.

In the test results from the COTELS project (Nagasaka *et al.*, 1999), it was found that water ingression through cracks/defects in core material interacting with concrete can contribute to coolability. Water can penetrate into debris at the sidewalls due to erosion at this interface as well as direct penetration of water into channels located in the central regions of the debris. However, there was no quantified data on the relative contributions of water ingression at the sidewall core/concrete interface versus ingression in the central core material region to the overall debris coolability.

Recently, Farmer *et al.* (2004) have reported the test results of the OECD-sponsored MCCI program on ex-vessel debris coolability and the two-dimensional molten core-concrete interactions under both wet and dry cavity conditions. They used fully oxidized 400 kg of PWR core melt, initially containing 8 wt. % calcined siliceous concrete in a specially designed two-dimensional siliceous concrete section. The core-concrete interaction results indicated that radial ablation is a key element of overall cavity erosion process. Late-phase flooding was found to cause a significant increase in upward heat flux from the debris. Crust breach by an insertable lance caused a dramatic increase in debris cooling rate.

Melt coolability research was also performed at the Sandia National Laboratory: SWISS (Blose *et al.*, 1987) and WETCOR (Blose *et al.*, 1993) experiments with stainless steel and corium melts respectively. High pressure corium quenching tests were performed in FARO facility (Magallon and Hohmann, 1995). A series of low temperature simulant material experiments were conducted by Theofanous *et al.* (1998) at the University of California, Santa Barbara.

Instead of top flooding of melt pool which showed limited contribution to coolability, another approach (bottom injection) was perused in the COMET project (Alsmeyer *et al.*, 1998). In the project, large scale (several hundred kilograms) melt pools were cooled and stabilized by injecting water at the bottom of the pool. This new approach works since it has been found that the injected water creates sufficient porosity in the melt pool to cool the melt in a relatively short time. Several experiments have been performed at different scales with Al_2O_3 and iron melt pools to prove the concept. The concept has been directed towards the design of a core catcher for a new containment design at FZK. The core catcher top face is made of some tens of millimeters of sacrificial concrete, under which nozzles are embedded in the basemat. These nozzles open when the concrete is ablated and inject water from the bottom into the melt pool. The COMET concept has been optimized through many experiments. No steam

explosions have been experienced. It appears that addition of the sacrificial concrete in the Al_2O_3–iron melt considerably reduces the explosivity of the melt.

Still in the coolability of melt pool, there are few experimental evidences to understand the melt pool coolability from the top or bottom;

(a) water ingression and melt coolability when the melt pool is flooded from the top in an ex-vessel situation
(b) the physical mechanism that creates porosity and melt coolability when the melt pool is injected from the bottom in an ex-vessel situation

1.1.4 Fuel-Coolant Interactions

The steam explosion loads on the containment were first considered in the WASH-1400 and, because of the assumptions made about the nature of this event at that time, the failure of containment (due to in-vessel steam explosion generated missiles) contributed a substantial fraction of the probability for early containment failure. The work on steam explosions, since that time, led to more realistic estimates of the probability of containment failure due to in-vessel steam explosions. A steam explosion review group (SERG) established in 1995 (SERG, 1995), deliberated on the phenomenology of the steam explosion and provided expert estimates on the probability of the containment failure as a result of an in-vessel steam explosion.

Much experimental and analysis-development work is in progress, presently, on in- and ex-vessel steam explosions. Experiments have been performed with less than gram quantities to several kilogram quantities of heated particles and molten materials. Elaborate three-field analysis codes: MC3D, IVA, ESPROSE.m and PM-ALPHA have been developed. Some of the insights gained are: (1) steam explosion probability is much reduced due to the extensive water-depletion that occurs around the fragmented particles of a jet in the pre-mixture; (2) super-critical steam explosions, however, cannot be excluded.

Ex-vessel steam explosion loads on LWR containments are also an issue, since (a) in some PWRs, water discharged from the reactor primary system accumulates in the reactor cavity under the vessel; and (b) in some BWRs, a deep water pool is established under the vessel, prior to vessel failure: an accident management strategy employed in the Swedish BWRs.

The ex-vessel water is generally highly subcooled and the extensive voiding, that develops in the pre-mixture in a saturated pool, may not occur in the subcooled pool. Additionally, it has been found that the median particle size, obtained during the break-up process, may be much smaller for the subcooled water than for the saturated water. Contrary to these effects, which may argue, on heuristic grounds, for a larger probability of a steam explosion, there are the effects of cooling and solidification which argue for a reduction in the probability of a steam explosion.

The corium melt may be a complex mixture of metals and oxides, however, predominantly it is a mixture of UO_2–ZrO_2–Zr, whose phase diagram, in general, shows a liquidus curve and a solidus curve, which are apart from each other by at most 200 to 300 K. For the UO_2–ZrO_2 mixture the difference between the liquidus

and the solidus curve is only 50–75 K. As the corium mixture solidifies its properties change radically. In particular, the viscosity, which is infinite in the limit of solidus, changes radically. The process of break up of a corium melt jet during its interaction with water results in many corium melt droplets of complex shape undergoing solidification from the exterior surface to the interior of the droplets. The changes occurring in the physical properties of the droplets affect the potential for the participation of the droplets in the steam explosion process. For example, it has been found that a thin high viscosity layer on the surface of a spherical droplet will greatly impede its subsequent fragmentation by a pressure wave, or shear forces.

The most remarkable experimental observations derived from the experimental program employing prototypic corium melt (UO_2–ZrO_2) in the FARO (Magallon et al., 1999) and (UO_2–ZrO_2) and Al_20_3 in the KROTOS (Huhtiniemi and Magallon, 1999, Magallon et al., 1999) facilities at Ispra, Italy.

It is clear that if a relatively large steam explosion occurs near the bottom of the 7 to 11 meters pool; the Swedish BWR containment (in particular the pedestal) can fail. It is also clear that the existing experiments, so far, indicate that the conversion ratio (or energetic yield) in a triggered UO_2–ZrO_2 explosion is significantly less than that in a triggered Al_2O_3 or stainless steel melt explosion. There are some 'limiting mechanisms' which reduce the yield for non-eutectic oxidic mixtures. In this context we still have to establish if the UO_2–ZrO_2–Zr mixture will behave differently from the UO_2 – ZrO_2 mixture.

These significant observations point to the important role that the melt physical properties may be playing in the steam explosion process. Much research on this aspect is being pursued in Europe under the auspices of the European Commission. Some physical mechanisms have been identified. However, no answer was yet given to the question on the role of the melt physical properties on energetics of steam explosions ('limiting mechanism').

In addition, relating to the coolability issues mentioned in the previous paragraphs, the information of melt debris size distribution due to steam explosion will be of importance to determine the configuration (for instance, debris porosity) of melt debris inside or outside the vessel relocated during severe accidents. The local fuel-coolant interaction produces fine debris less than centimeter in size. The produced fine particle buoyancies longer and settles on the top of the debris on the cavity floor, forming stratified corium debris bed which can be difficult to cool when coolant floods on it. Therefore, those are of critical information on the melt debris coolability;

(a) the governing mechanisms of energetic fuel-coolant interactions
(b) what extent the melt jet can be break up in relatively large debris enough to be cooled by flooded coolant,
(c) what extent the melt jet involved in the energetic fuel-coolant interactions and
(d) the formation of fragmented melt settled in the cavity.

1.2 Project Description

1.2.1 Project Objectives

The emphasis in this research is on the enhancement of coolability of porous corium outside of the reactor vessel due to incorporation of downcomers for both the particulate debris beds and the melt pools in the multi-dimensional aspects and on the understanding the mechanisms of fuel-coolant interactions and debris characteristics due to the fuel-coolant interaction.

The followings are the specific targets for the debris bed and melt pool coolability and fuel-coolant interactions.

Debris Bed Coolability (POMECO Program)

The influence of radial stratifications of the bed and non-condensable gases on the quenching using smaller size particles with prototypic porosity distribution and is investigated.

Melt Pool Coolability (COMECO Program)

The purpose of this work is to investigate and clarify the water ingression and melt coolability behavior when the melt pool is flooded from the top in an ex-vessel situation. Besides, the data are useful to validate mathematical models developed for water ingression phenomena during top flooding. Also, the results can be used for validation of computer codes used for light water reactors' severe accident analysis.

Fuel-Coolant Interaction (MISTEE Program)

The objective of this work is to investigate the mechanisms and energetics of energetic fuel-coolant interactions of metallic and binary oxidic melts to identify the effects of material properties using the single dope FCI facility with high-speed X-ray radiography and photography.

1.2.2 Project Work Description

Three different facilities for research under this topic, i.e., the COMECO (Corium Melt Coolability) facility, the modified POMECO (Porous Media Coolability) facility and the MISTEE (Micro-Interactions in Steam Explosion Experiments), are employed.

1.2.2.1 Ex-vessel Coolability of Particulate Debris Beds

The modified POMECO will measure the multi-dimensional distribution effects and the coolability of radially stratified particulate debris beds. No radially-stratified bed experiments and multiple water injection were performed in the POMECO facility, although axially-stratified beds were constructed and their characteristics measured. The purpose of the modified POMECO facility is to (a) add more downcomers in the debris bed to determine the interaction (b) add radial stratification of particulate debris beds and (c) determine multi-dimensional effects in coolability. The modified

POMECO facility will have the same test section of the POMECO facility with additional heaters and radially-stratified debris beds to realize the multi-dimensional configuration of the particulate debris beds which have different radial porosity and stratification. In addition, Water entry into the bed will also be made from the sides of the bed in order to have a 3-D distributive of cooling. The facility employs more temperature locations to measure the local temperature transient in multi-dimensional debris bed configurations.

In this modified POMECO facility, the bed was composed of sand with lower porosity layer of particles at the centre of test section and with higher porosity layer of particles at the periphery. The porosities and sizes of the sand particles chosen were close to those observed in a corium debris bed. The sand bed was heated volumetrically and was flooded with water from the top and from the bottom using downcomers. The quenching period for different conditions was measured and compared with that of a homogenous bed and axially stratified bed.

The other interesting phenomena are the effects of non-condensable gases on the quenching. For this, two different gases such as air and argon were injected at the bottom of the bed during the quenching conditions in order to understand the effects of gas properties on the quenching behavior. The gas flow rate was simulated to that actually generated during the later stages of MCCI from both basaltic and lime stone sand concretes. Experiments were conducted with and without gas injection rates when the bed was flooded from the top. The quenching behavior at different air flow conditions was studied

Specific phenomena associated with the configuration of radially-stratified porous debris beds with multiple water injection will be investigated; (a) quenching and dryout phenomena during top flooding, (b) effect of water injection at multiple locations at bed sides, (c) bottom flooding using downcomers, (d) effect of non-condensable gas injection, and compared the results with those of the previous debris bed experiments with homogeneous and axially stratified porous debris beds.

1.2.2.2 Ex-vessel Coolability of Melt Pool

Experiments were carried out in the COMECO facility to study the water ingression phenomena in melt pool and its coolability. The COMECO facility is employ one downcomer unit cell, while the modified POMECO can employ radially-stratified debris bed with multiple water injection and bottom flooding using downcomers, in order to observe any interaction effects.

The facility simulates the decay heat generated in the corium melt. The melt employed was a binary oxide mixture of 30% CaO+70% B_2O_3 (by wt.) which has glass type structure similar to the corium structure in the ex-vessel during the latter stages of accident progression when the corium melt is added with the reactor structural materials and interacts with the concrete basemat in the containment cavity. As a result, the melting point of corium is reduced and its viscosity increases significantly. Some of the data such as Modulus of Elasticity, tensile strength and linear thermal expansion coefficients are not available to make a direct comparison with that of the corium so as to assess its crack formation potential during quenching. However, some of its properties such as high viscosity, low melting point and glass

type structure are similar to that of corium during MCCI. About 14 liters of this melt was quenched in the facility with top flooding. The heat added to the melt by the four heaters was about 1.33 MW/m3 which is slightly higher than the decay heat. The melt temperature and steam flow rate were measured during the quenching process.

The COMECO facility also employs the TiO_2–MnO_2 melt, which has a different material structure than that of the CaO–B_2O_3 melt. It is believed that there may be differences in the water ingression efficiency in the melt pool due to material structure differences. The TiO_2–MnO_2 melt has a ceramic structure when it cools down, while the CaO–B_2O_3 melt is of glass structure as it cools. There are also differences in the viscosity of the two melts; the CaO–B_2O_3 melt has much higher viscosity.

The COMECO experiments are very difficult, time consuming and expensive since they are with high temperature melt, with special high temperature heaters around the test section supplying heat to the melt. The COMECO facility had leaks and we need to re-design it for greater durability and post-test access.

1.2.2.3 Ex-vessel Fuel-Coolant Interactions

The work in this task is important for the BWR containments in which a deep-water pool is established as an accident management strategy.

Since it is infeasible to perform large-scale steam explosion experiments with UO_2–ZrO_2 or UO_2–ZrO_2–Zr and it is very difficult to establish a scaling relationship, we believe that a more fundamental investigation will bear fruit in terms of identifying the mechanisms and energetics of fuel coolant interactions We accomplished this for the jet break-up phenomenon and now we have constructed the micro interaction steam explosion experiments (MISTEE) facility, wherein, currently, we are observing the differences between the character of the explosion phase of a steam explosion, for a single droplet, of different material (metal, single oxide, binary oxide mixture, binary oxide and metal mixture, etc.) melts. We obtain conversion ratio by employing a very fast pressure transducer. As experimental parameters, we will vary the subcooling of water, trigger strength and the melt droplet superheat.

A new medium-energy X-ray radiography system was developed at Royal Institute of Technology (KTH) in Sweden to visualize the fast transient multiphase and multi-component flow. This unique system replenished with capability of a continuous radiography at maximum 8000 fps by employing high-speed CCD camera. Therefore, this system is capable of observing the '*entire*' processes of fine fragmentation of a melt droplet during vapor explosion phenomena with '*consistent*' sequential visualization, which has never been achieved in the previous works. We applied this real-time continuous high-speed X-ray radiography to visualize the fine fragmentation process of molten melt drop to identify the FCI mechanisms in terms of various thermal and physical conditions as well as various materials.

Chapter 2
Coolability of Particulate Debris Bed

2.1 POMECO Experimental Facility

Figure 1 shows a schematic of the POMECO experimental facility. It basically consists of two stainless steel tanks with the lower tank being the test section and the upper tank is used for water over-layer for top flooding purpose. Both have the same cross-section of 350 mm square. The test section has a height of 500 mm and the height of upper tank is about 900 mm. A total of 7 downcomers were placed in the test section in order to bring water from the top tank to the bottom of the bed for bottom flooding purpose. The centre downcomer had larger size, with inner diameter of about 54 mm, as compared to the others. The smaller downcomers were having inner diameter of about 9.5 mm and they were placed at the periphery of bed as shown in Figure 2.

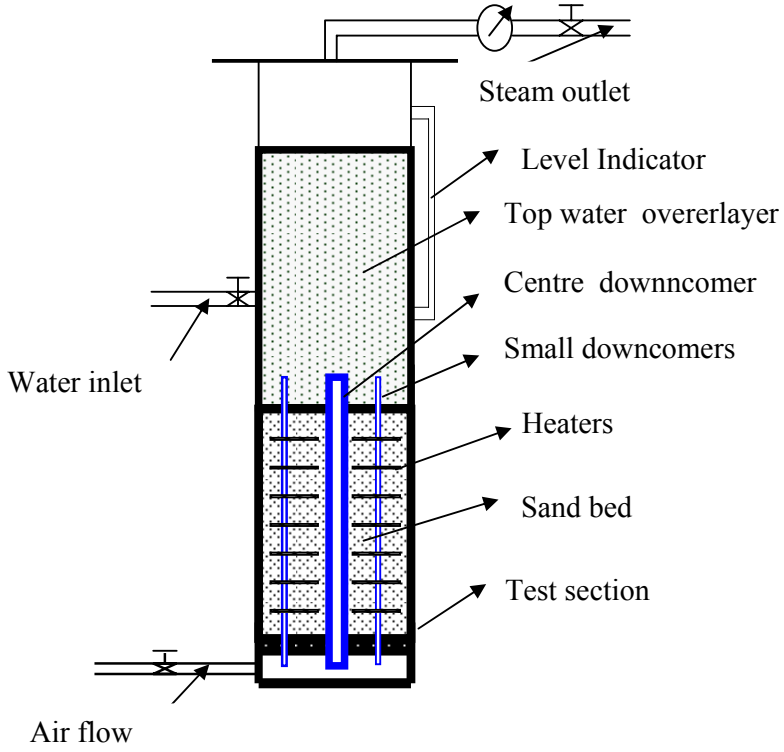

Figure 1: Schematic of the POMECO facility

The porous debris bed was simulated by using river sand particles with proper size distribution. The size and porosities of the sand particles used in the experiments were closer to that of the corium debris bed formed in an accident situation. We employed three types of sand in the present set of experiments as given in Table 1.

Table 1: Sand used for preparing the porous debris bed

Sand Samples	Size (mm)	Porosity (%)	Mean particle size (mm)
A	2 to 5	40.55	4.01
B	0.5 to 2	38.00	0.92
C	0 to 2	39.65	0.20

A mass mixture of A, B and C with proportion 7:7:6 yielded a sand composition with porosity of 0.26 and mean particle size of about 0.8 mm. The radially stratified bed was prepared by putting the high porosity sand (B) with porosity of 0.38 at the periphery and the low porosity sand of porosity 0.26 at the centre of the bed as shown in Figure 2. The thickness of the low porosity layer was almost equal to the sum of that of the high porosity layers. The sand bed is supported from bottom by a stainless steel net and another stainless steel net covers the top surface of bed to prevent the fly off of the sand particles from the bed. Provisions were made for supplying the non-condensable gases from the bottom of bed, which passes through the stainless steel net and sand bed. A schematic of the location of downcomers in the sand bed is shown in Figure 3.

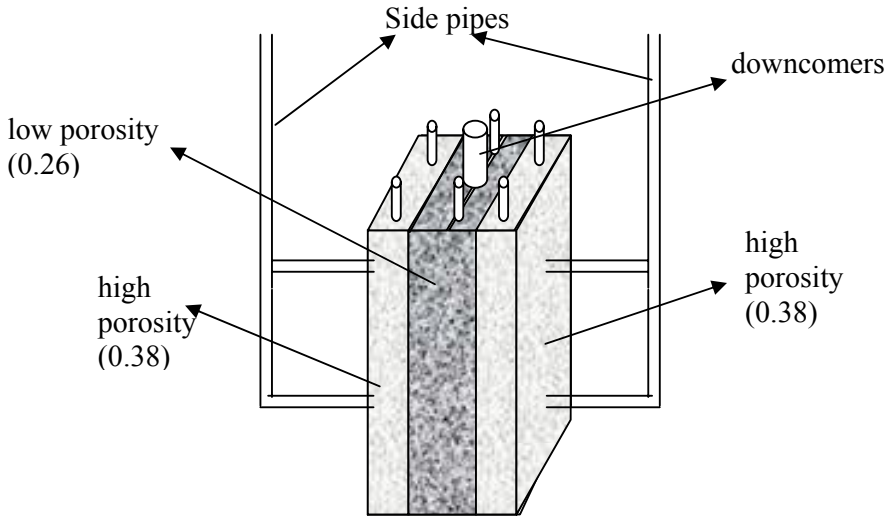

Figure 2: Schematic of the debris bed

The bed was heated almost uniformly by employing thin electrical heaters. In the test section of size 350 mm x 350 mm x 450 mm in which the sand bed was located, there were 24 heaters (having diameter 6 mm, material Inconel) used to heat the sand bed. The spacing between the layers of the heater rows was almost uniform (radially 25 mm and axially 35 mm). The heat generation rate in the heaters/unit length was the same in all the heaters. In fact, the test section looks like a forest of heaters if looked from top. The total capacity of the heaters is about 46 kW which corresponds to the volumetric power of 0.834 MW/m^3. This heat generation rate is nearly the estimated decay heat rate for the corium mixture.

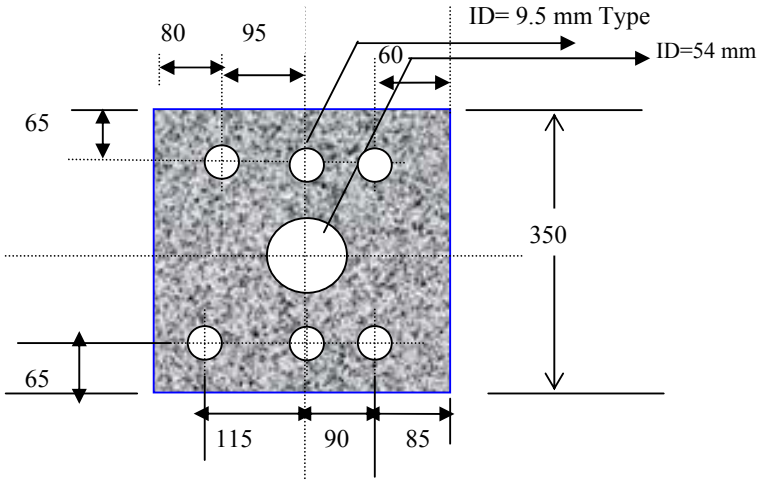

Figure 3: Schematic of location of downcomers in the bed

2.1.1 Instrumentation and Measurements

The most important measurement for this experiment is the temperature of the bed. For this we employed 48 K-type thermocouples, which were located at different planes as shown in Figure 4. For systematic measurement of bed temperature, the thermocouples were located symmetrically half on either side of the bed. We placed them at 8 different radial planes. Six thermocouples at different axial planes at a given radial plane are seen in the above figure. Hence, half of the thermocouples measure the temperature in the low porosity region and the remaining half measure the temperature in the high porosity region. In addition, the temperature of the feed water to the top tank and the steam temperature were measured. The steam flow rate was measured using a vortex flow meter. The air injection flow rate was measured using a variable area rotameter. The data generated from the thermocouples and the vortex flow meter was acquired using a HP data acquisition system.

2.1.2 Experimental Procedure

The POMECO experiments represent the later stages of the ex-vessel debris quenching during severe accident and after several hours when the corium starts attacking the concrete material. During this situation, the heat generation rate is nearly 10 % of the estimated decay heat rate of corium. The bed was initially heated to an average temperature of about 450 ^{o}C. The power input to the bed was kept at 10 % of full power (i.e. 4.6 kW) which corresponds to the estimated heat generation rate in the corium. The top of bed was flooded with water at 90 ^{o}C which can be the temperature of flooding water during an actual accident. During these tests the downcomers were closed. To study the effects of bottom flooding on quenching, downcomers were kept open. For this, we conducted tests with different combinations of downcomers in order to study the effects of their location and size on quenching. A list of experimental matrix is given in Table 2.

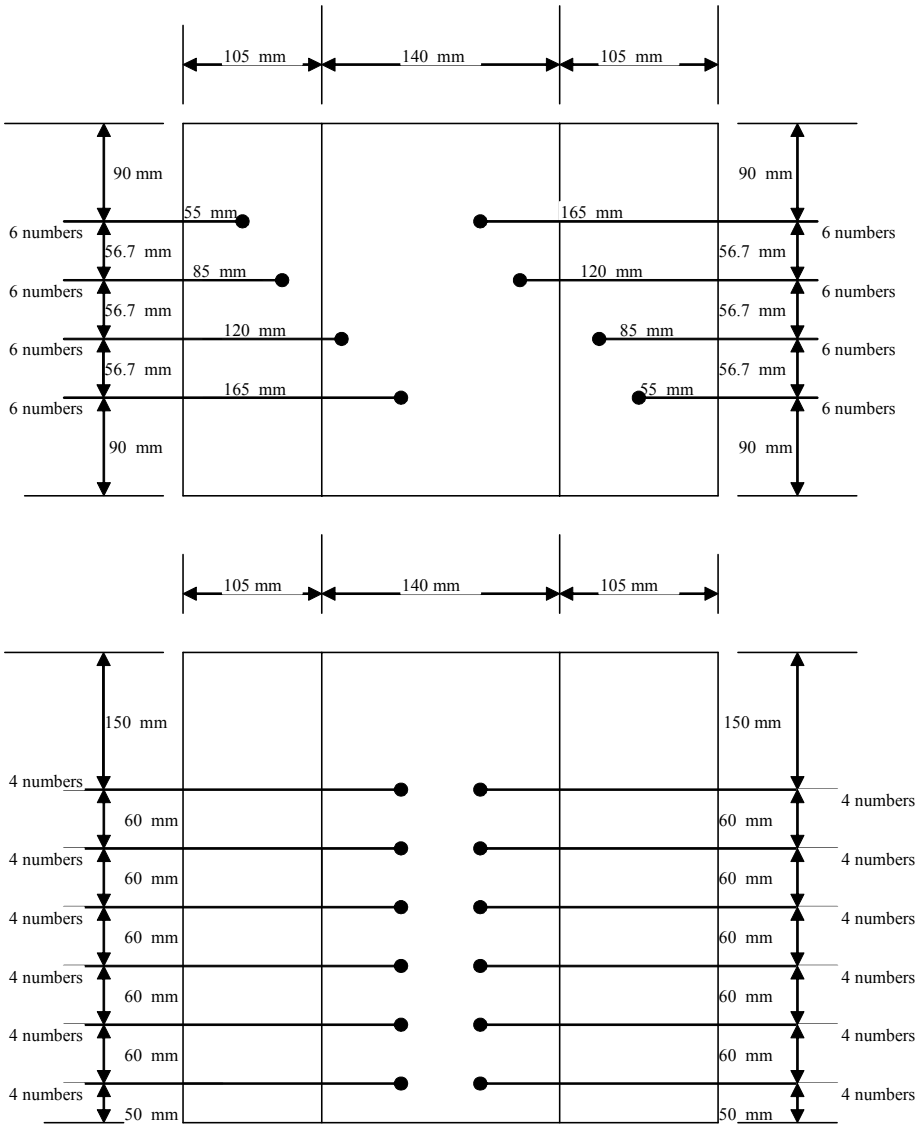

Figure 4: Location of thermocouples in the bed

During the MCCI in the later phases of transient, the concrete ablation rate is assumed to about 5 cm/hr, i.e. corium continues to penetrate the concrete at this velocity. The main contributors for the gas release in the concrete are carbon dioxide and water vapor, the amount of which depends on the concrete compositions, such as Basaltic Concrete or Limestone Concrete or CRBR Concrete. In this work, we simulated the gas release rates from two widely used concrete types (Basaltic and Limestone – common sand). We injected air at two different flow rates, i.e. 50 LPM and 125 LPM. These flow rates correspond to the gas generation rate in the basaltic and limestone common sand concretes respectively. The density of gas released during the MCCI is slightly heavier than air. To study the effects of gas density on quenching behavior, argon was injected at a flow rate of 40 LPM and 100 LPM respectively.

Table 2: Experimental test matrix for quenching for bed average temperature of 450 ^{o}C and flooding water temperature of 90 ^{o}C

Test No.	Downcomer	Air Injection	Argon Injection
1	No	No	No
2	Side pipes	No	No
3	Yes (centre only)	No	No
4	Yes (small six)	No	No
5	Yes (all seven)	No	No
6	No	50 LPM	No
7	Yes (Centre only)	50 LPM	No
8	Yes (Centre only)	125 LPM	No
9	Yes (Centre only)	No	40 LPM
10	Yes (Centre only)	No	100 LPM

2.2 Quenching Behavior of Debris Bed

2.2.1 Top Flooding

For the top flooding tests, all downcomers were closed in the facility. After the bed was heated to an approximate average temperature of around 450 ^{o}C, water at a temperature of around 90 ^{o}C was flooded to the top of bed. The height of water column above the bed was nearly 0.5 m, which was kept constant throughout the test.

Figures 5 (a) and (b) show the typical temperature history in the bed in the high and low porosities regions respectively. The initial bed temperature at the top and bottom regions was lower as compared to that in the centre of the bed due to heat loss. The time period for quenching was found to be higher in the low porosity region (about 5300 s) as compared to that in the high porosity region (about 4950 s). Previous experiments by Sehgal et al. (2001) have shown that for a homogenous bed with the porosity of 0.26 and mean particle size of 0.8 mm, the quenching period was about 1650 s for top flooding. When the porosity was larger (0.4) and the particle size was smaller (0.2 mm), the quenching period was about 9300 s, which is much longer than that with low porosity region. This implies that the quenching period is controlled more by the sizes of particle rather than the porosity.

The mean particle size of the low porosity sand and the high porosity sand was similar. Therefore the difference in quenching period was mainly due to difference in the porosities of the two layers. Moreover, it can be observed from the figures that the quenching behavior of the two layers are similar, i.e. the quenching first occurs at the top and then the front propagates to the bottom of the bed like that of a homogenous bed with top flooding. Hence there is no cross flow across the boundary between the two layers. This is similar to the observations made by Tung and Dhir (1987) for quenching in a radially stratified layer. However, in their experiments, they observed that the quench front moved very quickly to the bottom of the bed in the high porous region. After water accumulated at the bottom of the bed, an upward quench front is found to propagate in the low porous layer. It may be remembered here that the size of the particles used in the high porous layer (6.35 mm) was much higher than that used in the low porous layer (3.18 mm) in their tests. Hence there could be substantial

porosity difference among the high and low porosity layers of the bed unlike in the present case. That could be affected the quench front propagation seriously.

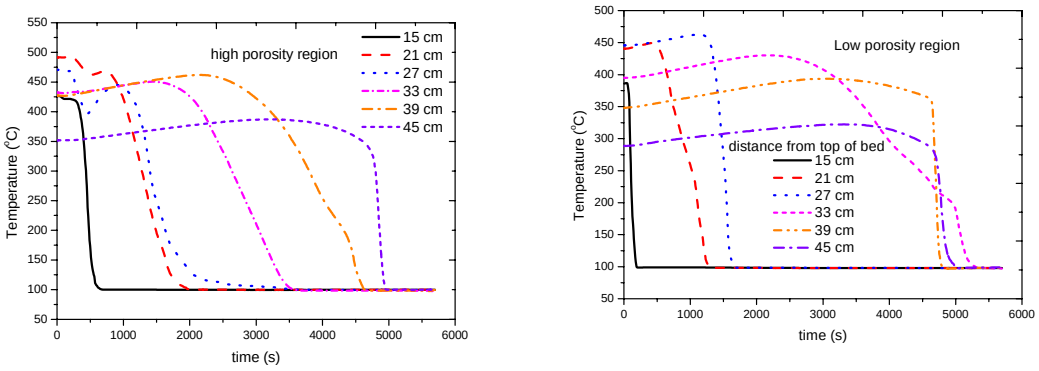

(a) (b)

Figure 5: Quenching behavior for top flooding

2.2.2 Non-Condensable Gas Injection

The effect of non-condensable gases on the quenching behavior with top flooding was studied which is shown in Figure 6 for the high porosity and low porosity regions. The air flow rate was about 50 LPM. The quenching rate is negligible as can be seen from the transient temperature history of the bed. Therefore the CCFL conditions exist both in the low and high porosity regions. The slight cooling observed at the bottom of the bed, mainly in the low porosity region, is caused by convection heat removal due to the low temperature air.

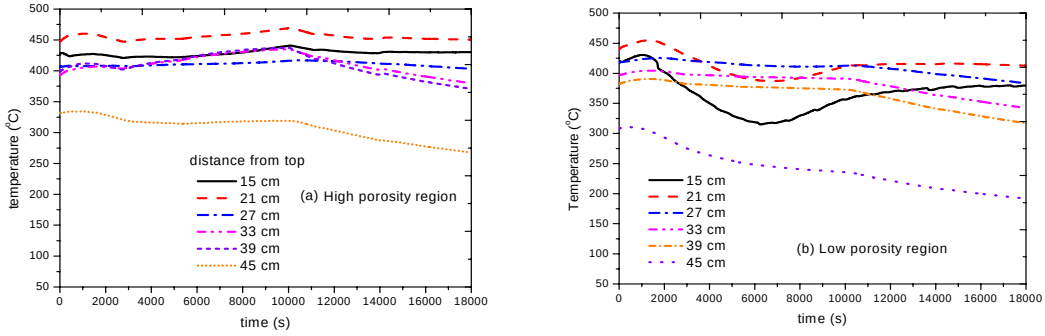

(a) (b)

Figure 6: Effect of non-condensable gas on quenching (top flooding, air flow rate is 50 LPM)

2.2.3 Top Flooding and Bottom Flooding with Downcomers

We investigated the quenching behavior of the bed with top flooding and bottom flooding using downcomers. First, the bottom flooding was carried out using the centre large downcomer only and the other six small downcomers were closed. Figures 7a and 7b show the typical temperature behavior of the bed during quenching for the high porosity and low porosity regions respectively. The presence of downcomer in the centre of the bed wherein the low porosity region is located helps in

better quenching. But the time for quenching in the low porosity region is still found to be longer than that in the high porosity region. Comparing these results with that of top flooding only, it is evident that bottom flooding helps in significant reduction of quenching period of the debris bed. Previous work by Konovalikhin et al. (2003) have reported a quenching time of nearly 1200 s for the homogeneous bed with porosity of 0.26 for the same mixture composition as used here. However, they employed a smaller downcomer with diameter 30 mm instead of 54 mm as used. Moreover, the use of a large size downcomer along with presence of a larger porosity region in the periphery of the bed has augmented the quenching rate. The quench front propagates downwards from the top due to top flooding and upwards from the bottom of the bed due to bottom flooding simultaneously. The centre region gets quenched at the end.

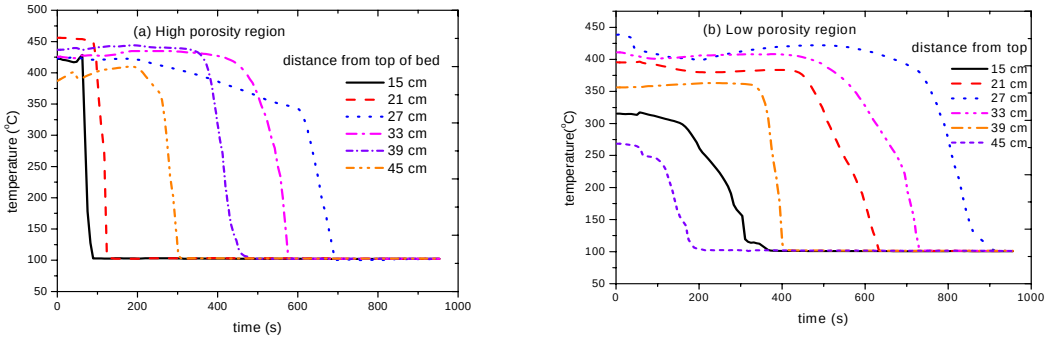

(a) (b)

Figure 7: Quenching with top and bottom flooding using center downcomer.

Next, we investigated the effects of size of downcomers and their locations on the quenching rate. So instead of using a large downcomer, we put six small downcomers of size 9.5 mm (ID) symmetrically in the bed as shown in Figure 2. These downcomers now are located at the periphery of the bed with two in the central low porosity region and two in each of the peripheral high porosity regions. The centre downcomer was closed. Figures 8 (a) and (b) show the temperature variation in the bed during quenching for the high porosity and low porosity regions for the same radial and axial locations as described before. The propagation of the quench front is almost similar to that of the previous case.

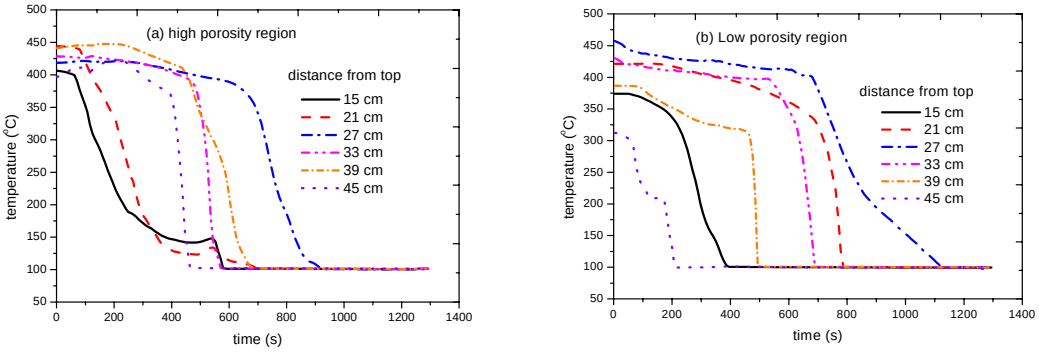

(a) (b)

Figure 8: Quenching behavior with top flooding and bottom flooding with small downcomers

The time period of quenching for both low and high porosity layers are higher as compared to the previous case. The combined flow area of the six smaller downcomers is smaller as compared to the centre large one. This may affect the bottom flooding rate and hence the quenching period.

On the other hand, employment of all downcomers together (i.e. the six small downcomers and the centre large one) reduces the quenching time further as shown in Figures 9a and 9b. Another interesting feature of this result is that the difference in quenching rate in the low and high porosity regions is much smaller unlike the previous cases.

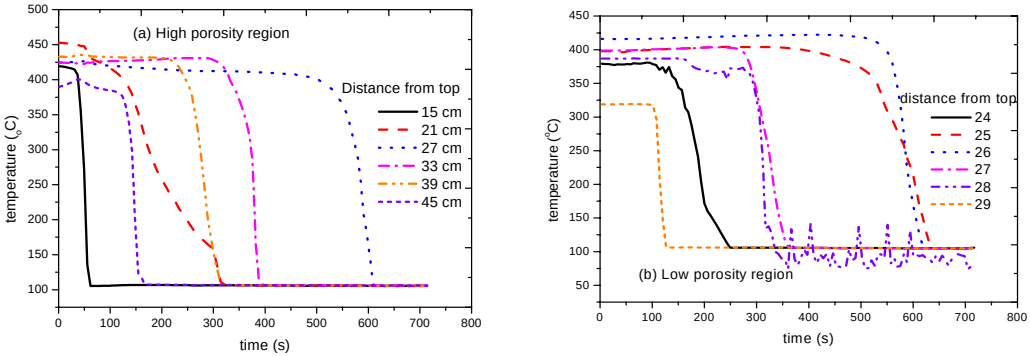

(a) (b)

Figure 9: Quenching behavior with top flooding and bottom flooding with all downcomers

Hence from the above results it is evident that the quenching of a heat generating radially stratified bed may not be effective with top flooding alone especially when the debris bed is generating non-condensable gases due to MCCI. The most effective means of quenching of the bed can be achieved by bottom flooding of the bed using downcomers in addition to the top flooding. These downcomers provide an effective passive means of removing the decay heat by two-phase natural circulation.

2.2.4 Non-Condensable Gas in Top and Bottom Flooded Bed

Next, it is of interest to investigate the quenching behavior of the bed when it is flooded from top and from bottom using the downcomer and when non-condensable gases are injected into the bed.

2.2.4.1 Air Injection

The effects of non-condensable gas on quenching during top and bottom flooding conditions were studied for different air flow rates. Figures 10 and 11 show the quenching rate for two different air flow rates, i.e. 50 LPM and 125 LPM in the high and low porosity layers, when the centre downcomer was open. There is a systematic increase in quenching time with increase in air flow rate observed at all axial locations in both high and low porous layers. The overall quenching time is also higher as compared to the case when no air was injected (Figure 7).

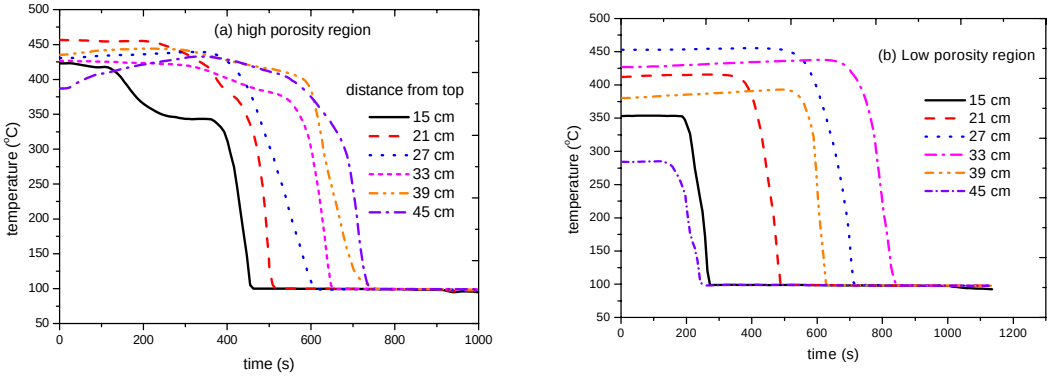

(a) (b)

Figure 10: Effect of the non-condensable gas on quenching (top flooding and bottom flooding with centre downcomer only), air flow rate is 50 LPM

The non-condensable gases trigger the CCFL and hence affect the flooding. One interesting observation here is that in the high porosity region, the quenching front propagates from top to bottom like the case with top flooding. It means, the air does not allow water to penetrate to the bottom of the bed. But in the low porosity region, the penetration of air into the bed is more difficult and hence it does not affect the quenching characteristics significantly. That is why at higher air flow rate, the quenching delay is more in the high porosity region as compared to that in the low porosity region. In fact at the air flow rate of 125 LPM, the quenching period in the high porosity region is found to be slightly longer than that in the low porosity region.

2.2.4.2 Argon Injection

In order to understand the effects of gas properties on the quenching behavior, we injected argon which is about 20 % heavier than air and repeated the quenching experiments with top flooding and bottom flooding with centre downcomer open only, which were already performed with air.

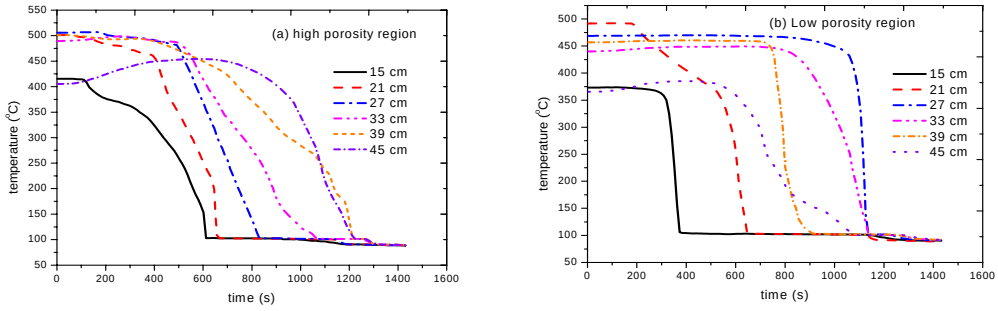

(a) (b)

Figure 11: Effect of the non-condensable gas on quenching (top flooding and bottom flooding with centre downcomer only), air flow rate is 125 LPM

Figure 12 shows the quenching behavior of the bed with Argon flow rate of 40 LPM in both low and high porosity regions respectively. This flow rate corresponds to approximately the mass flow rate for 50 LPM of air. The time period of quenching in the high porosity region was almost the same as that in the air where as in the low porosity region, the quenching rate with argon was found to be little smaller. Unlike in the low porosity region, the quench front propagation in the high porosity region was found to take place from top to bottom similar to that with air. The quenching rate in the top layer was also found to be smaller as compared to that in the bottom layers in the high porosity region.

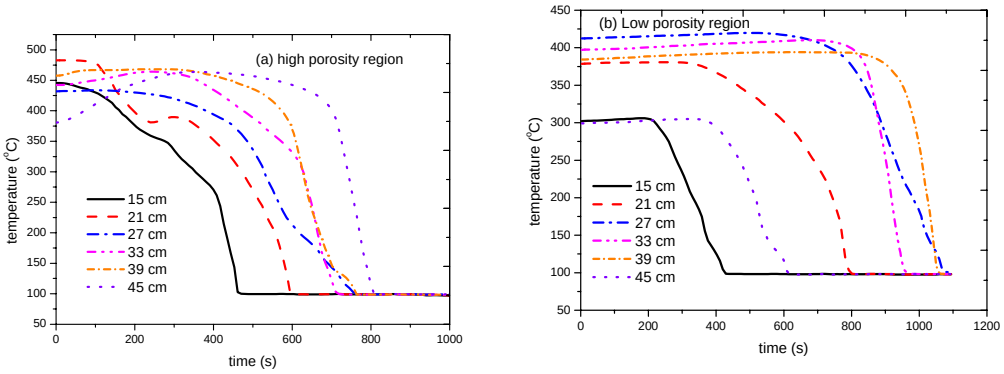

(a) (b)

Figure 12: Quenching behavior with argon injection (top flooding and bottom flooding with downcomer, argon flow rate of 40 LPM)

Figure 13 shows the quenching behavior of the bed when argon at a flow rate of 100 LPM was injected at the bottom of the bed. This corresponds to nearly 120 LPM of air. The time period of quenching was found to be longer than that observed with air both in the high and low porous regions. The quench front propagation was found to be similar like that of the previous case, i.e. flow rate of 40 LPM.

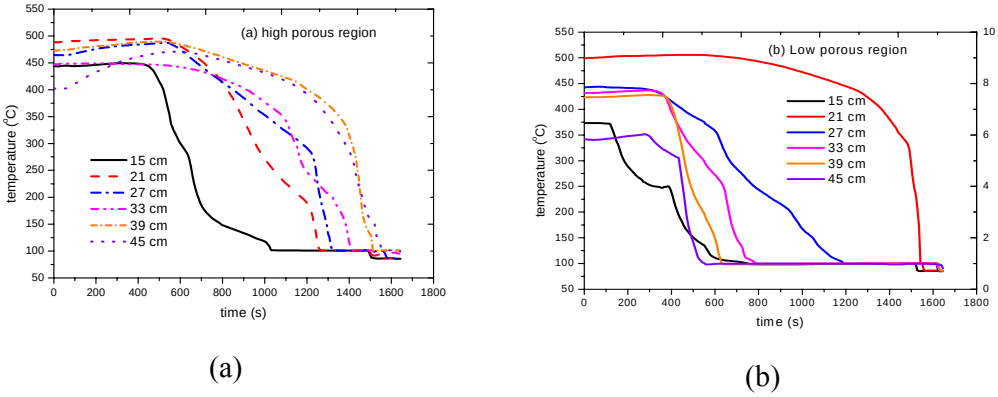

(a) (b)

Figure 13: Quenching behavior with argon injection (Top flooding and bottom flooding with center downcomer open only, argon flow rate of 100 LPM)

Moreover, it is found that higher the flow rate of the non-condensable gas, longer is the quenching period. Another interesting observation is that the quenching period for the top region is found to be longer in the high porous region as compared to that in the low porous region because of the non-condensable gases which prefer to flow in

the low resistant high porous region. Hence, there is more chance of CCFL in the high porous region for larger flow of non-condensable gases even though bottom flooding is done using a large size downcomer at the centre of the bed.

Chapter 3
Coolability of Melt Pool

3.1 COMECO Experimental Facility

The COMECO facility consists of a test section (200 x 200 mm cross section) with a maximum pool height of 300 mm. Figure 14 shows a schematic of the facility. The test section walls are made of carbon steel plates with thickness of 25 mm. The test section was connected to an upper tank whose height is about 1000 mm and cross-section same as that of the test section. The upper tank was used for water flooding purpose on the melt pool to the desired height. For this water preheated to a suitable temperature in the water storage tank, was delivered to the upper tank via the water line. The level of the water in the upper tank was kept at around 700 mm during the tests.

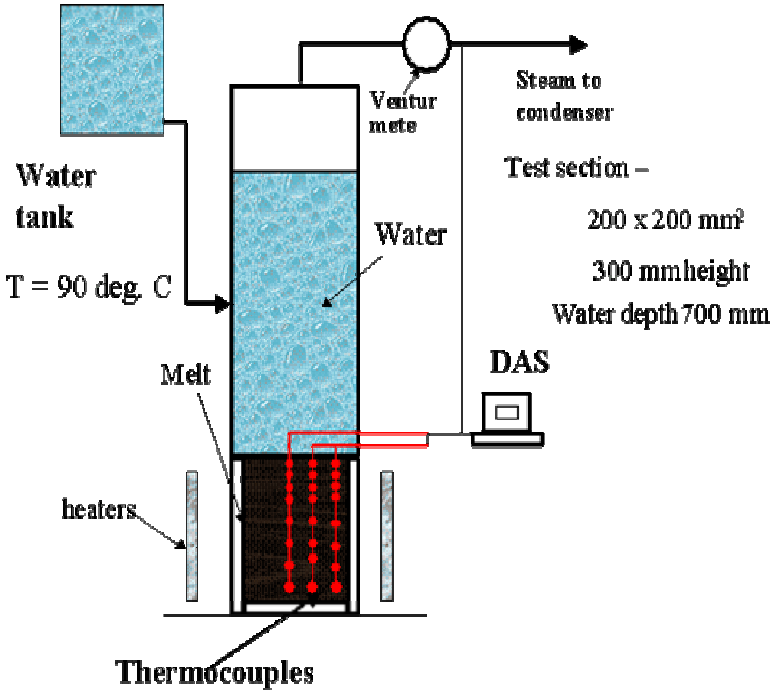

Figure 14: Schematic of the COMECO test facility

The melt employed was a binary oxide mixture of 30 % CaO + 70 % B_2O_3 (by wt.) which has glass type structure similar to the corium structure in the ex-vessel during the latter stages of accident progression when the corium melt is added with the reactor structural materials and interacts with the concrete basemat in the containment cavity. As a result, the melting point of corium is reduced and its viscosity increases significantly as said before. Table 3 shows the property of the CaO-B_2O_3 mixture. Some of the data such as Modulus of Elasticity, tensile strength and linear thermal expansion coefficients are not available to make a direct comparison with that of the corium so as to assess its crack formation potential during quenching. However, some

of its properties such as high viscosity, low melting point and glass type structure are similar to that of corium during MCCI. About 14 liters of this melt was quenched in the facility with top flooding.

Table 3: Property of ($CaO+B_2O_3$) mixture

Property	Value
Melting point (K)	1300
Density (kg/m^3)	2500
Viscosity (Pa.s)	0.1~0.3
Thermal conductivity (W/m-K)	3.0
Surface tension (N/m)	0.15
Specific heat (J/kg-K)	2200
Fusion heat (kJ/kg)	460

The melt pool was heated directly by heaters, located outside the test section on the four sidewalls. The heaters were made of Molybdenum silicate (MoSi) alloy that can be operated to a temperature of about 1700 ^oC. The four heaters could deliver the maximum power of 16 kW to the melt pool which corresponds to a heat generation rate of nearly 1.33 MW/m^3.

The most important measurement in this experiment is the transient melt pool temperature during the water flooding and quenching. The temperature in the melt pool was measured at different radial and axial positions. For this a total of 24 number of K-type thermocouples were employed at 3 radial planes (8 numbers in one radial plane) to record the transient temperature. The distribution of the thermocouples is shown in Figure 15. The steam flow rate was measured using a vortex type steam flow meter before it was condensed in the condenser.

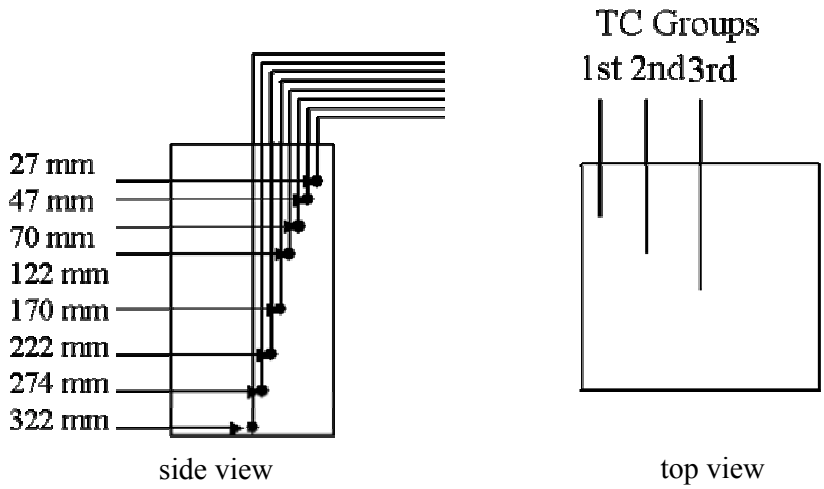

Figure 15: Schematic of the location of the thermocouples in the melt pool

3.1.1 Experimental Procedure

Before the experiment, the binary oxide mixture was heated up to a temperature of nearly 1300 ^oC in an induction furnace. This has a superheat of more than 250 ^oC above the melting point of the mixture. Before the melt was poured into the test section, the test section was heated to about 1100 ^oC in order to avoid the thermal

shock and deformation of the test section when the high temperature melt comes into contact with the test section.

About 14 liters of the melt was poured into the test section at the above temperature. This corresponds to an initial height of nearly 300 mm in the melt pool. Subsequently, water at a temperature of 30 ^{0}C was filled in the upper tank to a height of 700 mm in order to flood the melt pool from top. This height was kept constant throughout the test. The transient temperature in the melt pool and the steam flow rate were recorded using the DAS. The water temperature in the upper tank and the steam temperature were also measured.

3.2 Melt Pool Quenching

As said before, the COMECO experiments correspond to the latter stages of the accident progression. Figure 16 shows the temperature of the melt at various locations during the experiment. As we can see the temperature of the melt in the first three locations from the top reduces to almost to the saturation temperature of water very quickly. It is possible due to water touching the surface at the corresponding locations by ingression. The temperature at the fourth location from the top (which is about 122 mm) is also found to drop from the initial temperature due to heat conduction from the melt to the overlaying water. The water ingression was not observed at this location. Similar behavior is observed at locations below 122 mm. The rate of temperature drop was much smaller than that at 122 mm, which is due to additional heat transfer resistance to conduction heat transfer.

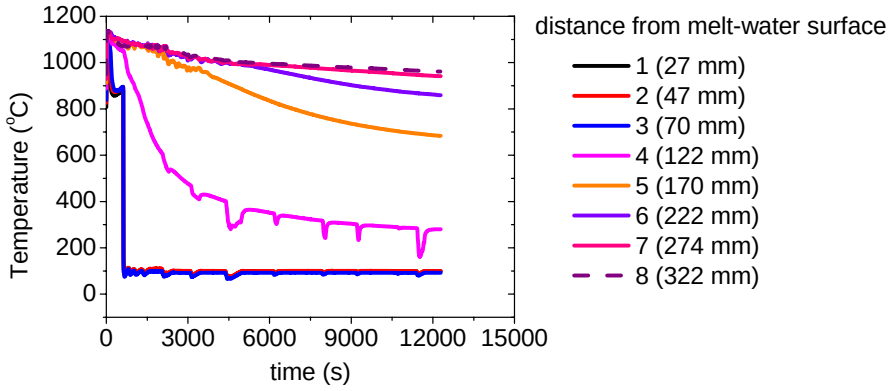

Figure 16: Temperature history during quenching of the melt pool (quenching occurs by ingression only up to 70 mm. Below about 122 mm, quenching occurs due to heat conduction only), but no water ingression occurs

Figure 17 shows the temperatures during the initial period of the experiment. As soon as the melt is poured into the test section, the temperature of the pool rises from the initial value. This further clarifies that the melt is completely poured into the vessel and touches almost all the thermocouples. The moment the melt pool is flooded with water from top, the temperatures of the first three thermocouples drop almost together gradually. Once the water is able to touch the surface, the temperature drops quite suddenly as seen from the figure.

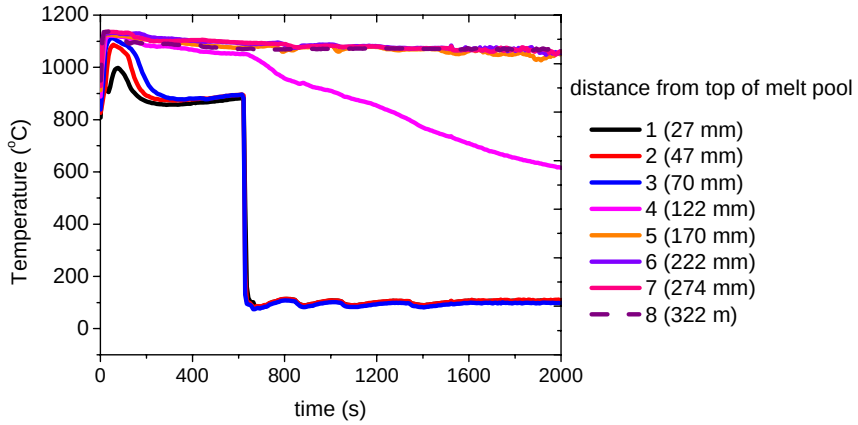

Figure 17: Temperature history during the initial period of quenching.

Figures 18 and 19 show the temperatures of the melt at the other radial positions, deeper inside the vessel. They also exhibit similar quenching behavior as in the first radial position which is closer to the wall. In Figure 16, the temperature at a location of 122 mm from the top was found to exhibit some oscillations. This probably happens when the subcooled water (at temperature of 30 ^{o}C) was added to the upper tank periodically to maintain the level. When the subcooled water is added the heat transfer increases from the melt pool to the water thereby causing a temporary decrease in the melt temperature.

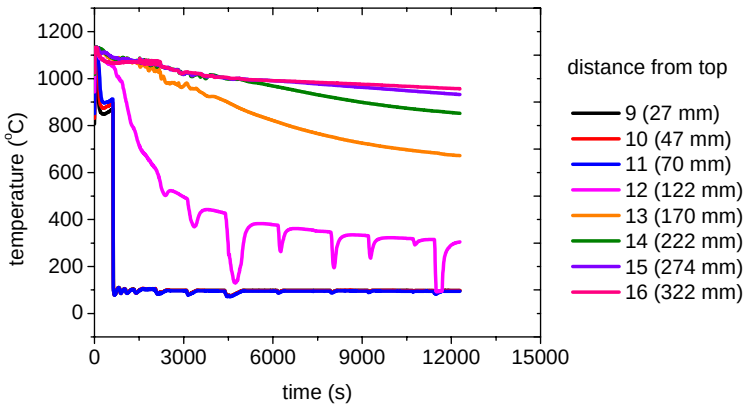

Figure 18: Temperature history in the melt pool at radial distance of 80 mm from wall

Figure 20 shows the steam flow rate measured during the experiment. The flow rate is high during the initial quenching process and later on decreased to a very low value. After the test was over, the crust formed was examined for its structure. Figure 21 shows a structure of the crust at the top of the bed. As it can be seen, a lot of fragmented pieces were observed at the top which was mainly due to the break-up of the crust. The fragmented pieces were found up to a depth of nearly 100 mm from the top of the pool. This further confirmed that water could ingress only up to this depth. Beyond this the crust was found to have a rock like structure without any porosity as shown in Figure 22. Water could not ingress into this structure. The heat transfer to the overlaying water from this was mainly by conduction as said earlier. That is why

the temperature of the melt pool was found to drop very slowly below the depth of 70 mm from the top.

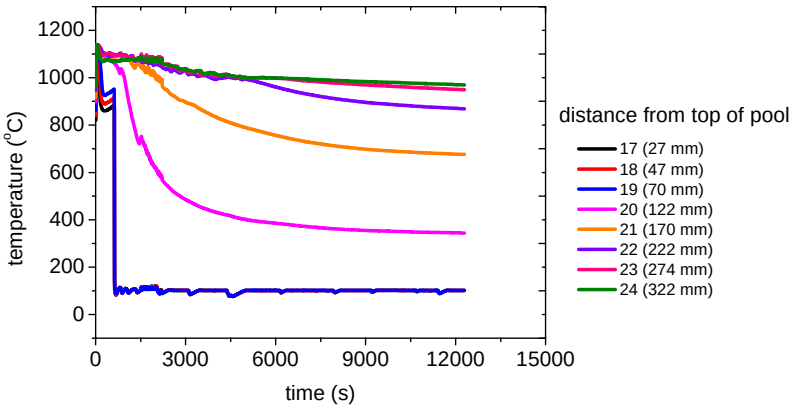

Figure 19: Temperature history in the melt pool at radial distance of 100 mm from wall

It should be noted that water ingression in melt pool occurs due to crack formation during the melt quenching and solidification process and it should be a function of the melt structural properties such as Modulus of Elasticity, tensile strength and coefficient of linear expansion and physical properties such as its solidus and liquidus temperature, viscosity, thermal conductivity, etc.

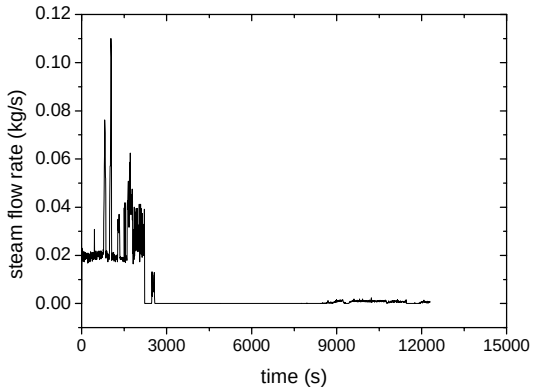

Figure 20: Steam flow rate during the quenching

As said before, we are discussing the phenomenology in the ex-vessel situation during the later stages of the severe accident progression. The viscosity of the corium will be substantially higher and its melting temperature will be lower as compared to that of the initial stages due to the addition of the structural materials and its interaction with concrete. The results suggest that it is difficult to quench the melt below a depth of 70 mm. The corresponding dryout heat flux estimated based on the heat removal rate to the water over-layer from the 70 mm thick melt pool which was cooled and it was found to be about 93 kW/m^2.

Figure 21: A view of the structure of the crust at the top of the pool

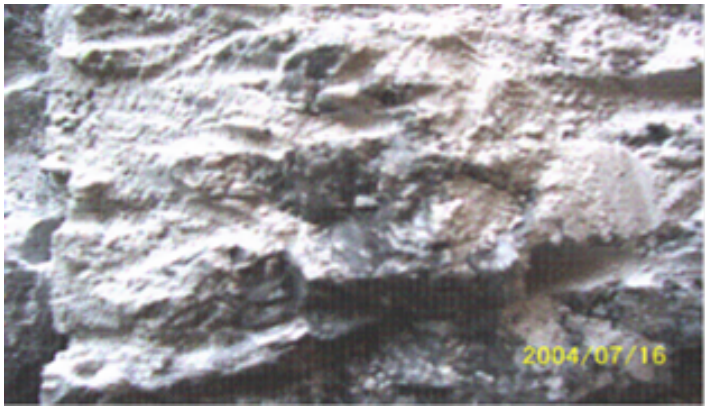

Figure 22: A view of the structure of the crust cut axially from top to bottom

It may be noted that in the SSWICS results, the dryout heat flux was measured and predicted to be about 200 kW/m^2 for concrete concentrations of about 8% by wt. and 75 kW/m^2 for concrete concentrations of about 25% by wt. in corium (Farmer *et al.*, 2003). These results are similar to that observed in the present case. Hence, even though the melt employed here is a simulant and its properties are not exactly the same as corium as discussed earlier, nevertheless, these results are important for the considerations of water ingression and melt pool coolability in light water reactors.

Chapter 4
Energetic Fuel-Coolant Interactions

4.1 MISTEE Experimental Facility

A facility, called MISTEE (Micro Interactions in Steam Explosion Experiments) with a continuous high-speed X-ray radiography system is used for the single drop vapor explosion and shown in Figure 23.

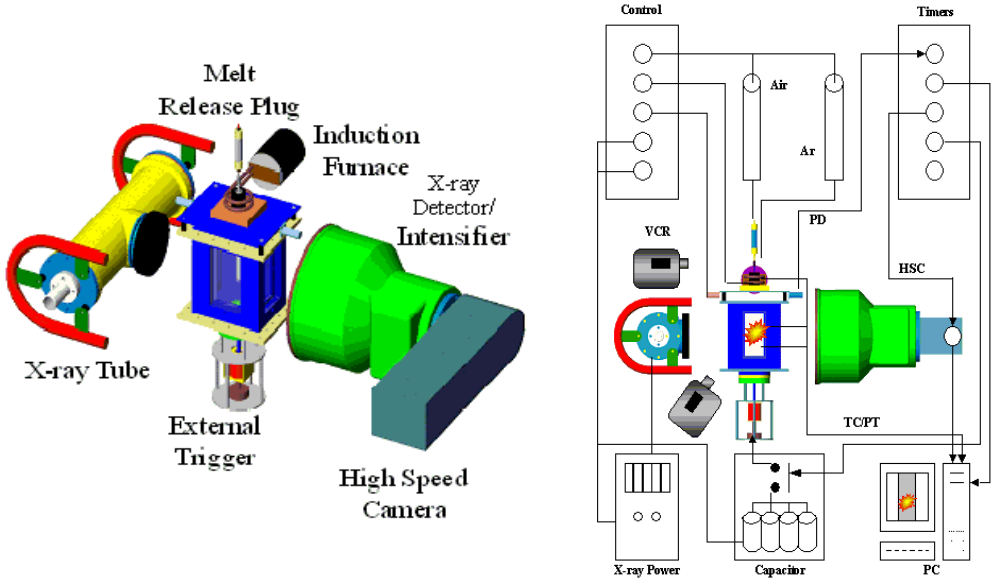

(a) (b)

Figure 23: The schematic diagrams of (a) the MISTEE facility and (b) the control system. LS: Laser, PD: Photo Detector, HSC: High-Speed Camera, TC: Thermocouple, and PT: Pressure Transducer

The MISTEE system consists of: an interaction chamber, an induction melt furnace, an external trigger system, an operational control system, and data acquisition and visualization systems. The test section is a rectangular stainless steel tank (180x130x250mm) with 4 view windows (70x150x 24mm) and a 1kW immersion heater at the bottom. A piezoelectric pressure transducer (PCB Piezotronics 102A03, sensitivity 75.0mV/MPa, rise time < 1.0μs or 102A04, sensitivity 750mV/MPa) is flush-mounted on the center of a test section wall. The pressure transducer is connected to the four-channel ICP signal conditioner (PCB Piezotronics 442A04).

K-type thermocouples are used to measure temperatures of the molten droplet at the furnace and water temperature inside the test section. The pressure transducer is connected to the four-channel ICP signal conditioner (PCB Piezotronics 442A04). Furnace with the voltage and current up to a 260V and 40A, respectively, consists of a graphite cylinder (40mm OD x 50mm) and an alumina crucible (20mm ID x 30mm)

with a 4.1mm hole at the center of the bottom. A Boron-nitride plug (10mm OD x 20mmH) as a melt release plug is used to block the crucible bottom hole during the melting and is lifted by a pneumatic piston to release the melt drop. The external trigger, located at the bottom of the water tank, is a piston that generates a sharp pressure pulse similar to a shock wave. The trigger hammer is driven by a rapid discharge of a capacitor bank consisted of three capacitors ($400V_{dc}$ and 4700 mF each) that impacts on the piston to generate a pressure pulse.

The visualization system, photography and radiography, consists of a continuous X-ray source tube (Philips continuous X-ray, MCN 323) with the maximum voltage of 320 keV and the maximum current of 22mA, an X-ray converter and image intensifier (Thomson TH9436 HX) with a view window of 290mm and a high-speed video camera (Redlake HR2000 Motion Scope) with the maximum recording time of 4 seconds at the maximum frame rate of 8000. The X-ray converter and image intensifier powered by a high voltage power supply (Thomson TH 7195) has three different magnification modes.

X-rays are detected on the input phosphor screen with a CsI crystal layer and converted into photoelectrons that are accelerated, amplified and converted at the output phosphor screen to visual light. The resolution of the X-ray image is 56 line pairs per centimeter. The image size of the high-speed camera at 8000 fps is 80x70 pixels.

The MISTEE facility is located inside reinforced-concrete containment (3.8m x 3.8m x 3.9m) with a thickness of 600 mm, for the X-ray radiation shielding during the tests. The operation of the test is controlled remotely outside the containment. The schematic diagram of the control system is also shown in Figure 23b.

4.1.1 Experimental Conditions and Procedures

In the present tests, molten tin (Sn) and normal tap water were used as a high-temperature liquid and a cold liquid, respectively. Figure 24 illustrates the experimental conditions in a Thermal Interaction Zone (TIZ) plot for tin-water system (Nelson, 1981). The temperatures of melt and water were set to about 1000 °C and a range of 20 ~ 90 °C, respectively. A 0.7g molten tin drop was chosen to ensure the delivery of a single drop into water through the crucible bottom hole. The thermal initial conditions as shown in Figure 24 cover unstable and stable regions of the TIZ. All tests were externally triggered before the possible spontaneous explosion even when the initial thermal conditions were in the unstable region of TIZ.

The experiment starts heating up the tin in the induction furnace. The molten drop is released into the test section filled with water by the remote operation of lifting the melt release plug. In the case of the X-ray radiography tests, X-ray is turned on before the release of molten drop. When the released tin drop cuts a horizontal line laser beam (ELFA TIM201) located below the furnace and 100 mm above the water surface, a laser beam sensor (ELFA BPX43-3) detects the laser beam disturbance and then provides a reference trigger signal to the remote control system. A set of timers (1ms time resolution) in the control system provides trigger signals at different times to operate the subsequent automatic sequences, such as triggering of: the high-speed camera, the data acquisition system, and the external trigger system.

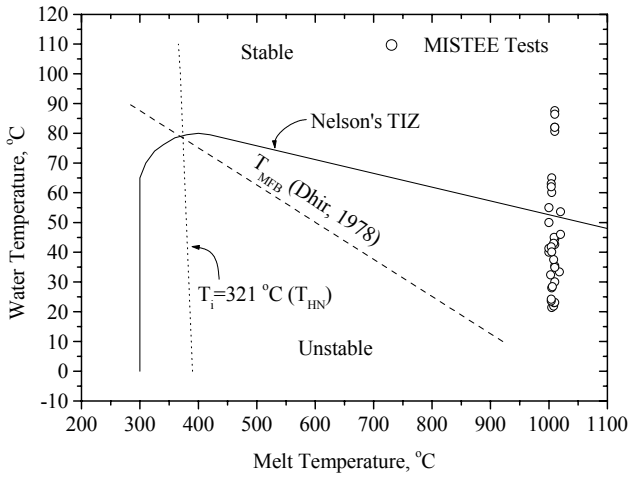

Figure 24: Experimental conditions in the thermal interaction zone (TIZ)

The vapor explosion is initiated by a shock wave generated from the external trigger system attached beneath the test section. Recorded images are downloaded into a PC where the post image processing takes place. A commercial image process software (Optimas 6.1 in Media Cybernetics) and MATLAB software with the image-processing package are used to analyze the image data.

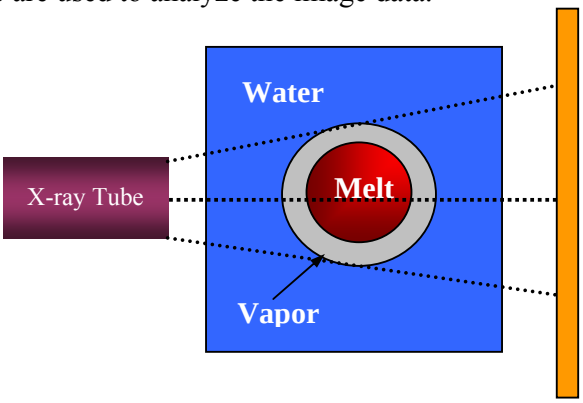

Figure 25: The schematic diagram of the X-ray Radiography

4.1.2 Image Processing Techniques

The intensity of the detected X-rays, I, after obeys the attenuation law as follows

$$I^{NS} = I_0 \exp\left\{-\sum_i \mu_i \delta_i\right\} \tag{1}$$

where, I^{NS}, δ_i and μ_i are the detected X-ray intensity without scattering in the surrounding media, the thickness and the mass attenuation coefficient of i-th materials. Therefore total X-ray intensity detected at the converter consists of the X-ray intensity without scattering, I^{NS}, and the X-ray intensity with scattering I^{S},

$$I = I^{NS} + I^{S} \tag{2}$$

This transmitted X-ray beams are proportionally converted into photon beams at the converter, which are recorded into contrast images by the high-speed CCD camera in

our radiography system. The image contrast proportional to the transmitted X-ray beam is transformed into digitized gray level. Therefore the digitized gray level, G, can be expressed as,

$$G = CI + G_{DC} = C\left(I^{NS} + I^{S}\right) + G_{DC} = CI_0 \exp\left\{-\sum_i \mu_i \delta_i\right\} + G^0 \tag{3}$$

where C, G_{DC}, and G^0 are the proportional constant, dark current of the image system and the image offset which represents the background noises of the image gray level due to the scattered X-ray beams and the CCD dark current.

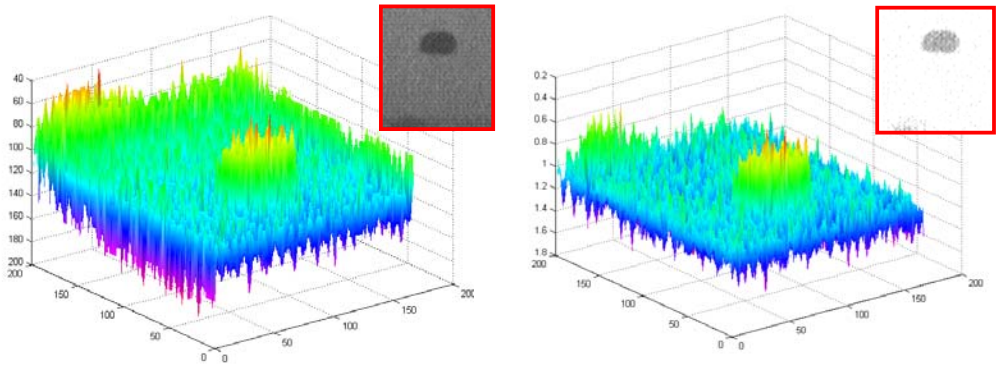

(a) (b)

Figure 26: Image enhancement: (a) original image and (b) enhanced image

The basic arrangement of our XR system (X-ray tube and converter) with a test section that has multiphase mixture of water, vapor and melt during the vapor explosion process is shown in Figure 3. In this configuration, the X-ray intensities with and without melt droplet surrounded by vapor film, G_M and G_{NM}, respectively can be obtained as follows

$$G_M = C_M I_0 \exp\{-\mu_A \delta_A - \mu_{TS} \delta_{TS} - \mu_L \delta_{LM} - \mu_V \delta_V - \mu_M \delta_M\} + G_M^0 \tag{4}$$

$$G_{NM} = C_{NM} I_0 \exp\{-\mu_A \delta_A - \mu_{TS} \delta_{TS} - \mu_L \delta_L\} + G_{NM}^0 \tag{5}$$

where the subscripts A, TS, L, LM, and V are denoted as the air, the test section, the liquid pool, the liquid pool with a melt droplet and the vapor. Since the projected area of the melt droplet in the test-section filled with liquid is significantly smaller than that of the test-section, $C_M \sim C_{NM} \sim C$, $G^0_M \sim G^0_{NM} \sim G^0$ and $\delta_{LM} \sim \delta_L$ will be valid. In addition, since the attenuation of X-ray beam in the vapor film around the melt droplet is negligible, the equations (5) and (6) becomes

$$G_M \cong CI_0 \exp\{-\mu_A \delta_A - \mu_{TS} \delta_{TS} - \mu_L \delta_L - \mu_M \delta_M\} + G^0 \tag{6}$$

$$G_{NM} \cong CI_0 \exp\{-\mu_A \delta_A - \mu_{TS} \delta_{TS} - \mu_L \delta_L\} + G^0 \tag{7}$$

Combining the equations (7) and (8), the normalized gray level of the image can be expressed in terms of the thickness of the melt droplet as

$$\begin{aligned} \frac{G_M - G^0}{G_{NM} - G^0} &\cong \exp\{-\mu_M \delta_M\} \\ &= \gamma \exp\{-\mu_M \delta_M\} \end{aligned} \tag{8}$$

where γ is a constant determined by a series of calibration tests. Finally, the thickness of the melt droplet during the vapor explosion process can be obtained by,

$$\delta_M = a + b\ln\left(\frac{G_{NM} - G^0}{G_M - G^0}\right), \text{ where } a = \frac{1}{\mu_M}\ln\gamma \text{ and } b = \frac{1}{\mu_M} \tag{9}$$

4.1.3 Melt Thickness Calibration

A series of calibration tests was conducted with tin foils with the various thicknesses of 0.025, 0.05, 0.075, 0.25, 0.5, 1.0 and 2.0 mm. The calibration tests were performed by inserting tin foil (7mm x 7mm) with known thickness into the center of the test section filled with water. The gray level ratio, $(G_M - G^0)/(G_{NM} - G^0)$ is obtained by taking dark current image for G^0 and images with and without the object of interest for G_M and G_{NM}, respectively. It is noted that G^0 taken during the calibration process contains only the CCD dark current. In the present tests, scattered X-ray intensities with and without melt droplet in the test section, i.e., I^s_M and I^s_{NM}, will not be significantly different each other since the size of the melt droplet is considerably smaller than that of the test section. Therefore, during the calibration process to obtain the gray level ratio, this scattering noise can be eliminated from the images. Figure 26 shows the image enhancement after the process, indicating significant reduction background noises.

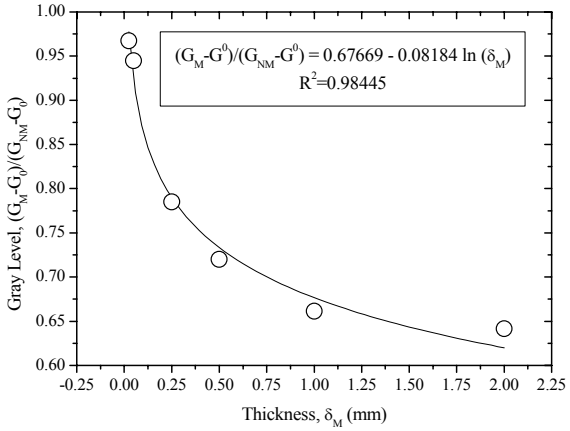

Figure 27: Calibration curve for the melt thickness

Figure 27 is the final calibration curve to convert the gray images taken by X-ray radiography to the quantitative distribution map of the fragmented melt particles. The resulted calibration curve is given by

$$\frac{G_M - G^0}{G_{NM} - G^0} = 0.67669 - 0.08184\ln\delta_M \text{ with } R^2=0.98445. \tag{10}$$

The non-uniformity of the background is due to the camera noise (dark current), uneven illumination through the image (output screen response and intensity distribution of X-ray radiation – maximum in the center) and CCD response to light (each pixel response varies). That means that the background subtraction and offset correction should be performed pixel by pixel and not using an average number.

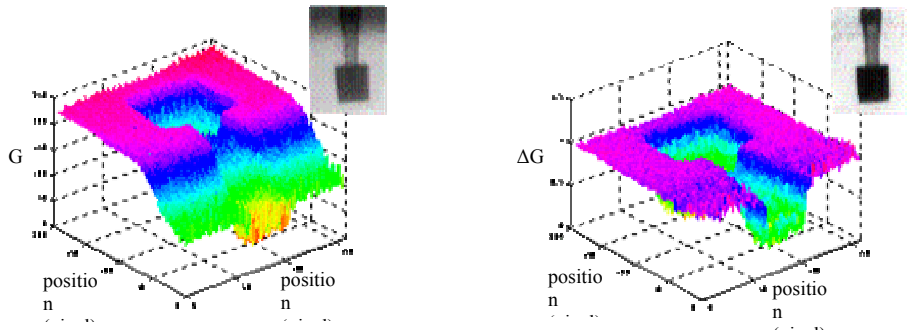

(a) (b)

Figure 28: (a) tin phantom gray level; (b) tin phantom after image processing

Figure 28a shows the brightness distribution of the radiography image of a tin piece, and Figure 28b shows the same image after G^0 correction. It is clear the significant reduction of the image noise, has been achieved.

- Fluctuation of the optical brightness between pixels $\Delta\varepsilon_{pixel}$
- Contrast ratio on the fluorescent screen $\Delta\varepsilon_{screen}$
- Deviation between the actual and measured thickness, $\Delta\varepsilon\delta$
- Statistical error of the X-ray beam $\Delta\varepsilon_{stat}$

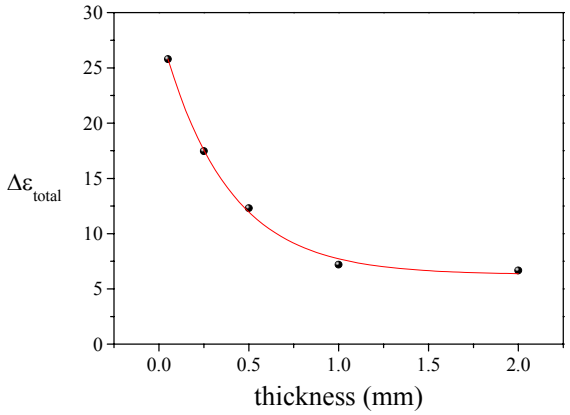

Figure 29: Total uncertainty of the measurement.

The achievable measurement accuracy depends on the statistical error of the X-ray beam $\Delta\varepsilon_{stat}$, contrast ratio on the fluorescent screen $\Delta\varepsilon_{screen}$, on the fluctuation of the optical brightness between pixels $\Delta\varepsilon_{pixel}$, and the deviation between the actual and measured thickness, $\Delta\varepsilon_{\delta}$. The correlation for the total uncertainty $\Delta\varepsilon_{tot}$ is given by:

$$(\Delta\varepsilon_{tot})^2 = (\Delta\varepsilon_{stat})^2 + (\Delta\varepsilon_{screen})^2 + (\Delta\varepsilon_{pixel})^2 + (\Delta\varepsilon_{\delta})^2 \qquad (11)$$

As shown in Figure 29, for a higher thickness the error decreases, this can be explained by the fact that the optical brightness approaches its saturation, represented by the asymptotic part of the calibration curve, giving an almost constant gray level. For the thinner phantom, scattering becomes significant since it creates a loss of contrast even after the G^0 correction.

Figure 30 compares the thickness of a melt drop before vapor explosion assumed to be a spherical shape (dotted line) and actual calibrated thickness of the same drop (dot). The calibrated thickness of the droplet closely reproduced the horizontal drop size of approximately 10 mm and the thickness of the drop. In fact, noises such as regular grid-shape TV lines in the image produced the fluctuation of the thickness of the drop. The solid line was obtained by performing a FFT smoothing technique with adjacent 15 points. The additional noise reduction techniques will be required to reduce the error of this quantitative measurement.

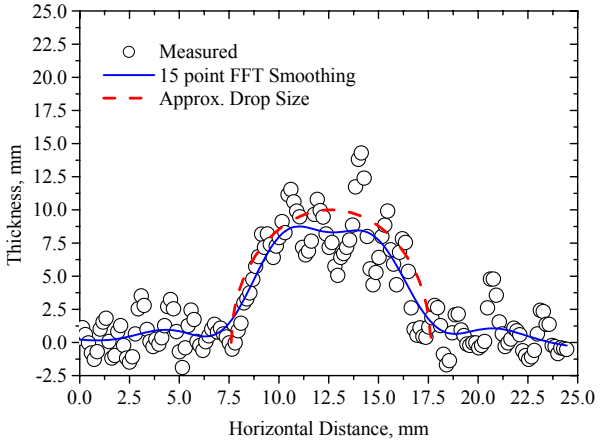

Figure 30: Calibration of X-ray image gray level to actual thickness of molten tin droplet prior to the triggered vapor explosion

4.2 Fuel-Coolant Interactions in Single Drop

4.2.1 Melt Drop Penetration in Subcooled Water

The molten tin drop freely falls into the water surface. The photographic images showed that the drop was a near-spherical shape during the falling in the air, because of the surface tension force is much more important than inertia force. The impact velocity on the water surface at present conditions; i.e., a 3~5 mm diameter tin drop falls over a falling height of 110 mm in the air, was about 1.45 m/s.

Figure 31 shows the drop trajectory in water. It tells us that the falling velocity of the molten droplet was approximately 0.4 m/s in water. The drop falls in water with an oscillatory motion from a spherical shape to an ellipsoidal spherical-cap shape. Most of tests show that the ratio of maximum horizontal diameter to the initial diameter of the drop is about 2. The drop does not break up during the falling, since the Weber number of the drop was much smaller than the critical Weber number of 12. Figure 31 indicates that, in the period of vapor explosions, the drop falling speed estimated at the center of mass of fragmented particles reduces from 0.4 m/s to less than 0.1 m/s. A group of fragmented particles after the vapor explosions gradually falls down with a speed of about 0.3 m/s. This trajectory of the molten tin drop is quite consistent with all tests.

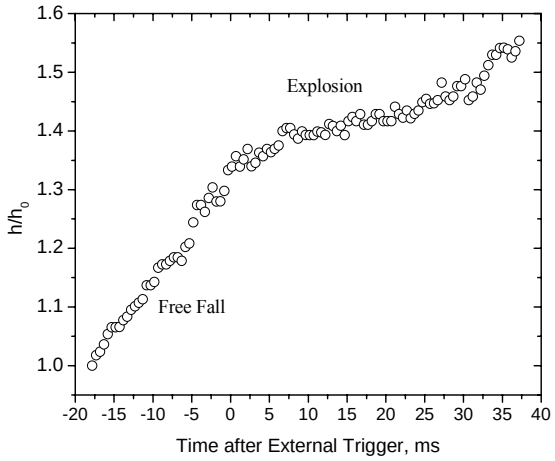

Figure 31: Molten tin drop trajectory

Figure 32 shows a typical pressure history of the tests. Time zero was denoted as the time when the external trigger signal arrived at the center of the test section where the vapor explosion takes place. Most tests employed approximately an external trigger of 1 MPa with a rising time of less than 50μs. Major pressure pulse, generated by vapor explosions, reaches the pressure transducer approximately 4 to 5 ms after the trigger shock disturbed the quasi-stable vapor film around the droplet. The vibration of the test section due to the impact of the external trigger piston and reflection waves of pressure signals caused the sinusoidal fluctuation (frequency of ~ 1 kHz) of the pressure signal.

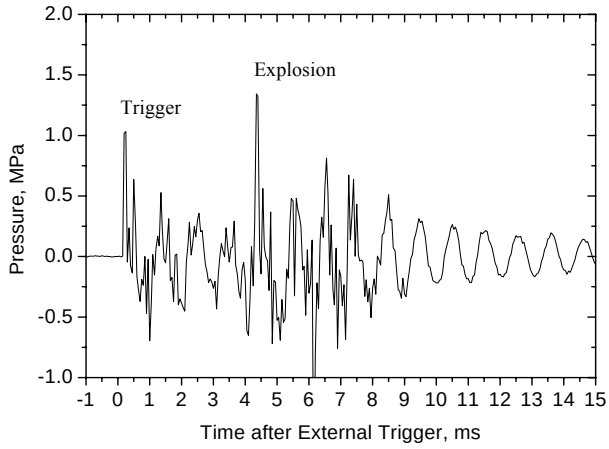

Figure 32: A typical pressure history for triggered vapor explosion of 0.7g tin drop at 1000 ^{o}C in water at 21 ^{o}C.

4.2.2 Visual Observation by High-Speed Photography

Images of vapor explosion recorded by high-speed X-ray radiography and photography at 8000 fps are shown in Figure 33. The time shown is normalized to t_c, the duration time for the first bubble or melt fragmentation growth and collapse estimated from the high-speed images for each test. Time t=0 for the images was set for the first disturbance of the bubble or melt by the impulsive shock observed from

the high-speed images for each test. The trigger shock wave propagates up to the melt drop from the bottom of the images.

Two sets of high-speed photographs in Figure 33 were taken at water temperatures of 32 and 45 ^{o}C. At t/t_c=0.1, the melt drops for both tests were already disturbed by the trigger shock wave, showing cavitations of vapor/gas pocket on the top of the melt droplets. Obviously, at lower subcooled water, the size of vapor/gas pocket was larger than that at highly subcooled water. At t/t_c=0.8, vapor at the bottom of the melt drop collapsed into the melt, initiating major explosions. During the explosions, wavy boundary of vapor was clearly observed.

There are three interesting observations: vapor/gas pocket collapse, high-speed fragment jet ejection and secondary explosion from relatively larger size of melt fragments. These observations were widely reported in previous research works. However, those have some values which provide some clues of understanding the melt fragmentation behavior observed by X-ray radiography in this work. First, for the collapse of the vapor/gas pocket as shown at t/t_c=2.3, the test in 45 ^{o}C water shows that the large vapor/gas pocket attached on the top of the melt drop was completely collapsed into the explosion interaction zone. In fact, the collapse increases the amount of non-condensable gases, originally entrapped during the impingement into water, in the interaction zone. This increment of non-condensable gases could delay heat transfer process and eventually reduce the energetics of vapor explosion (Akiyoshi, 1990).

Second, after t/t_c=2.3, the ejection of fragment jets were clearly observed. These jets had a maximum velocity of about 9 m/s and were ejected from the wavy boundary of the interaction zone. These jets can be an evidence of a micro-jet formation, similarly observed in the cavitation process when a bubble approaches a rigid wall. Lindau and Lauterborn (2001) found that the counter-jet, with a velocity of approximately 16 m/s, appeared at 14 μs after a liquid micro-jet grew on the opposite side of the bubble surface against the rigid wall. Lastly, secondary explosions of large melt fragments was observed as shown at t/t_c=4.3. The melt fragments were separated from the wavy surface of the interaction zone as similar to the secondary breakup (Pilch, 1987) and exploded. This secondary explosion was not observed in tests with water temperature less than 40 ^{o}C.

4.2.3 Visual Observation by X-ray Radiography

The X-ray radiographs shown in Figure 31 were performed at the same melt thermal conditions, but with different water temperatures up to 82 ^{o}C. The X-ray image at t/t_c=0.1 shows that the melt droplets have a near spherical shape. The deformation of melt surface at the bottom of the droplet is observed at t/t_c=0.8, which indicates the triggering of vapor explosions by the impulsive external trigger. For the test with 21 ^{o}C water, explosion triggered at the edge of the droplet and propagated along the melt surface which is similar to a stratified mode of vapor explosion. This type of the triggering was observed in most of the highly subcooled water tests. For the lower subcooled tests, explosion triggered at the bottom of the drop surface generating melt jet fingers beside the local trigger point. Local high vapor pressure generated at the location of vapor collapse squeezes the melt surface and produces a crater on the drop

surface. The stratified explosion at t/t_c=2.3 for the highly subcooled test, fragments the drop around its surface and leaves a long elongated filament of melt.

For the lower subcooled tests, a counter melt jet appears at the crater and ejects in the radial direction from the drop surface. At the same time, the top surface of the drop starts showing ripples and another explosion occurs, supposedly from the collapse of the vapor/gas pocket into the melt drop. In particular for 82 ^{o}C water test, the disturbance of the top surface of the melt drop was clearly observed. At t/t_c = 0.8, two melt jet on the top surface of the melt were rebounded believably due to the collapse of the vapor/gas pocket. This disturbance leads to relatively weak explosion in this test afterward.

X-ray radiographs at t/t_c=3.0 illustrates that the melt fragments expands in the radial direction and forms a shell of melt fragments. During the fragment shell formation, no significant amount of melt was observed at the center of the shell. For the 65 ^{o}C water tests, the explosion induced at the top was even stronger to push the fragmented melt particles downward, forming a empty region on the top. The images for the higher water temperature tests clearly indicate that explosions occurred at two different locations, i.e., at the bottom surface by the external trigger and at the top surface by the vertical collapse of the vapor/gas pocket. Therefore, the collapse of the vapor/gas pocket at the lower subcooled water causes two counter effects on the single drop vapor explosion: suppressing the vapor explosion by supplying condensable vapor and non-condensable gases (increase in void fraction) into the interaction zone and triggering vapor explosion.

At t/t_c=3.0, the images show that melt fragments are redistributed into the center of the initial melt location due to the collapse of the vapor bubble. These images illustrate that most of the fragmented melt particles stay in place although the vapor bubble interface collapses.

4.2.4 Dynamics of Vapor Bubble and Fine Fragments

Figure 34 illustrates the time evolution of radial vapor bubble and fragments of 0.7 g molten tin drops at 1000 ^{o}C for different water temperatures. Our data was also compared with Nelson's data for 0.05g of iron oxide at 1960 ^{o}C in 30 ^{o}C. In this figure, the equivalent bubble diameter, D_{eq} (area averaged diameter for the melt drops), is normalized with the equivalent diameter of the melt drop prior to the external trigger shock wave arrival.

The maximum bubble diameters reached about 3~3.5 times the initial bubble diameters mostly after the third cycle of bubble growth-collapse. For the iron oxide melt, however, the bubble diameter expanded to about 8 times the initial diameter. The first bubble growth and collapse takes 1.125, 1.375, and 1.25 ms at water temperatures of 32, 45 and 82 ^{o}C, respectively, which are similar to Ciccarelli's data (Ciccarelli, 1991) with 0.5 g tin at 700 ^{o}C. The distribution diameter of melt fragments, at 42 ^{o}C water, completed the first cycle at 1.5 ms. The first cycle of bubble dynamics for the iron oxide took similarly about 1.0 ms. The cycle periods after the first cycle varies from 1.0 to 2.0 ms, since these periods strongly depend on the subsequent fine fragmentation process.

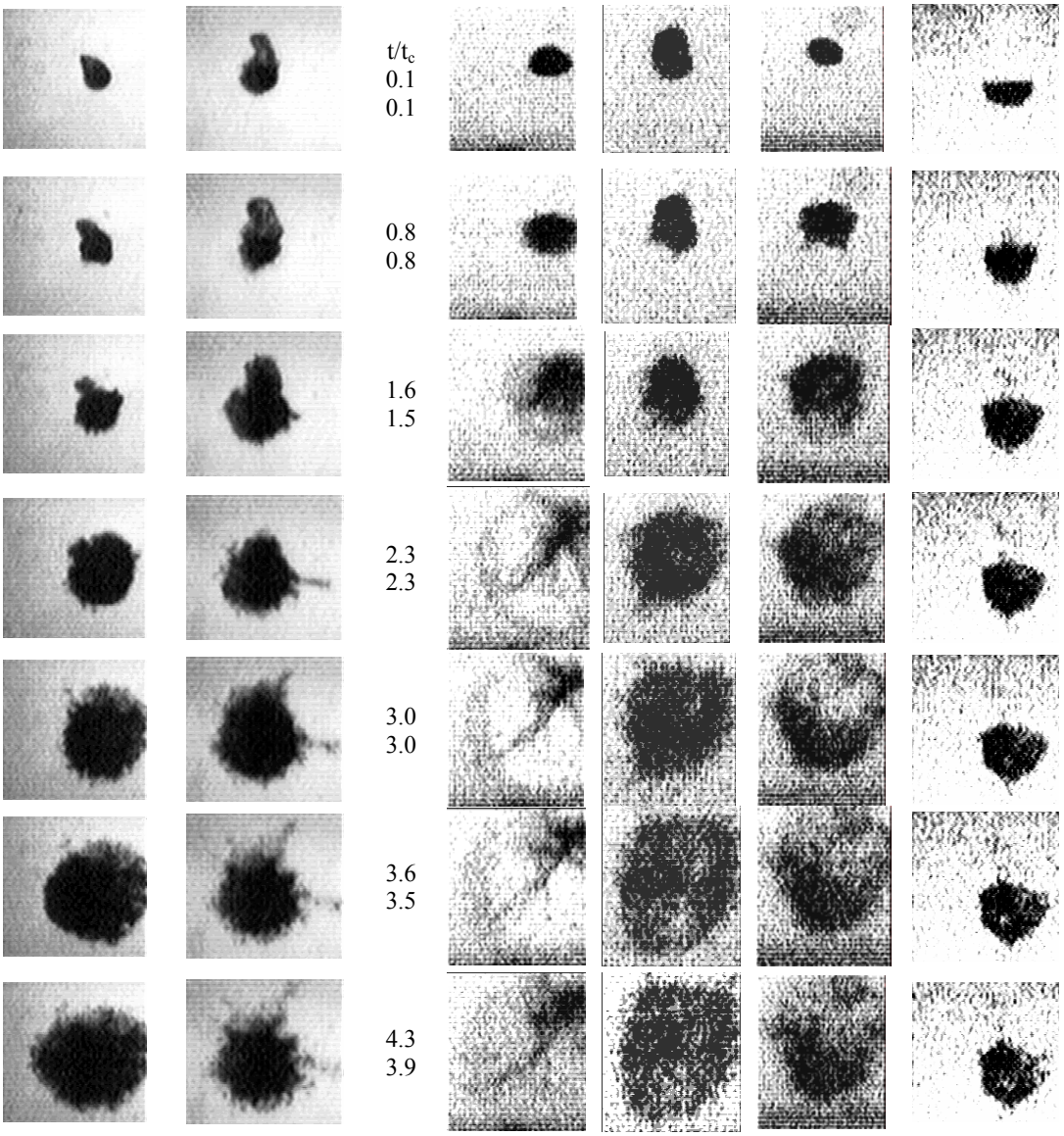

Figure 33: Selected photographs (left) and X-ray radiographs (right) of the vapor explosion of 0.7g tin drops at 1000 °C in different water temperatures.

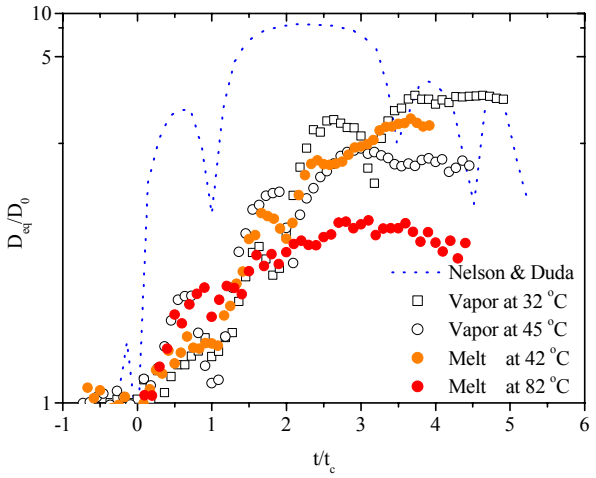

Figure 34: Time evolution of vapor bubble and melt fragments of 0.7g tin droplet at 1000 °C in water at 32, 42, 45 and 82 °C

4.2.5 Transient Distribution of Melt Fragments

Figure 35 shows the original, processed, and calibrated X-ray radiographs at 22 °C water. The thickness of the melt fragment distribution was calibrated as mentioned in the previous section. The calibrated thickness of the melt fragments shown in this figure is, in fact, the line-off-sight averaged thickness of melt-fragments positioned along the projected line of the incident X-ray beam. These contour maps of the 2D projected melt mass distribution show that the thickness of the fragmented melt clouds, during the melt expansion, becomes thinner. However, the thickness of the fragment shell stopped at the vapor boundary becomes thicker. At t/t_c=4.3, the melt fragments are redistributed due to the vapor collapse, showing thicker concentration.

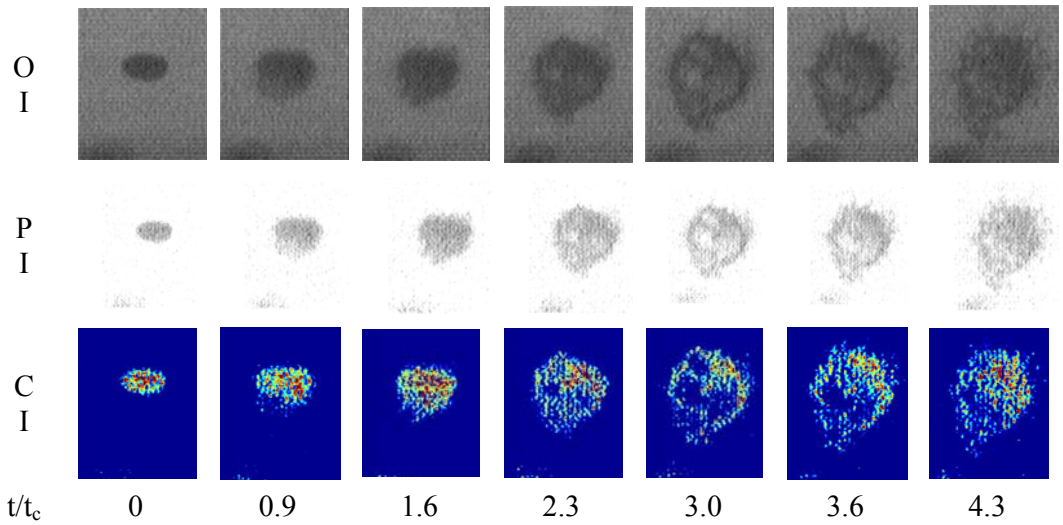

Figure 35: X-ray radiographs (right) of the vapor explosion of 0.7g tin drops at 1000 °C in 22 °C Water. Image size for the original radiographs is 29.3x24.6mm (199x167 pixels). OI: Original Image, PI: Processed Image, CI: Calibrated Image

Figure 36 is the radial mass distribution of melt (thickness) at the center of mass of the fragmented melt particles shown in Figure 35. The figure clearly shows the radial expansion of the melt mass, peaking at the vapor boundary and lowing at the center region of the melt. In fact, the plots indicate that conservation of total mass estimated at each time step is rather poor because of significant noises in the images. Therefore, for more accurate quantitative analysis, further efforts on image noise reduction are required.

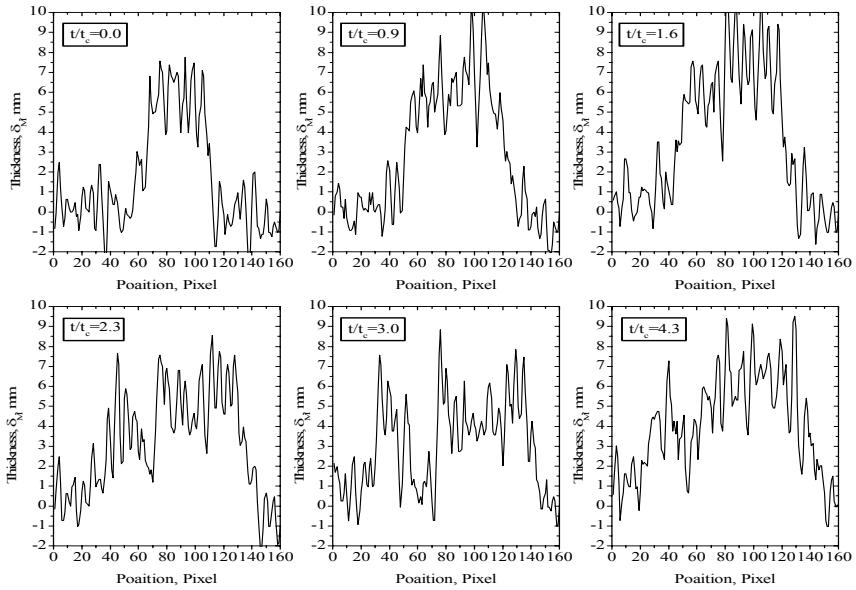

Figure 36: Transient distribution of line-off-sight averaged thickness of a tin drop.

4.3 Energetics of Fuel-Coolant Interactions

The energetics of single drop fuel-coolant interactions resulted from the bubble dynamics which is fueled by the explosive heat transfer between the fragmented molten droplets and surrounding cold and volatile liquid. The periodic violent bobble growth and collapse generates pressure pulse as shown in Figures 32 and 34. In the MISTEE, a fast response pressure transducer measures the dynamic pressure resulted from the FCI bubble dynamics and high-speed photograph images provide the radial bubble volume dynamics. Both quantified data can be used to evaluate the energetics of single drop fuel-coolant interaction without knowing the internal heat transfer mechanisms. However, combing the melt dynamics visualized by the X-ray radiography with those data eventually enables to identify the relationship between the melt fragmentation and corresponding vapor bubble dynamics.

First for the evaluation of the bubble dynamics, one single bubble model as shown in Figure 37 is considered. The momentum equation combing with mass equation is give as,

$$-\frac{1}{\rho}\frac{\partial P}{\partial r}=\frac{1}{r^2}\frac{\partial F}{\partial t}-\frac{2F^2}{r^5} \text{ where } F(t)=R^2\frac{dR}{dt} \tag{12}$$

By integrating in the far field, r>>R, pressure in liquid at r can be written as

$$P(r,t) - P_0 = \left(\frac{\rho_l}{4\pi r}\right)\frac{d^2V}{dt^2} \tag{13}$$

Bubble volume (or radius) can then be obtained by integrating Eq. (13) as given below,

$$V(t) = \left(\frac{4\pi}{3}\right)R^3(t) = \int_0^t\int_0^\tau\left(\frac{4\pi r}{\rho_l}\right)\left(P(r,t) - P_0\right)dtd\tau \tag{14}$$

Internal bubble pressure can be obtained from the classical Rayleigh-Plesset equation as expressed below,

$$P_v(t) - P_0 = \rho_l R\ddot{R} + \frac{3}{2}\rho_l R^2 + \frac{4\mu_l}{R}\dot{R} + \frac{2\sigma}{R} \tag{15}$$

The energetics of fuel-coolant interaction is conventionally measured by a conversion ratio which is defined as the useful mechanical work done by a FCI bubble volume onto the surrounding liquid to the total initial internal energy of a melt drop. Therefore the conversion ratio can be given as follows,

$$\eta(t) = \frac{W}{E_t} = \frac{\int_0^t\left[\left(P_v(\tau) - P_0\right) - \sigma\frac{A(\tau)}{V(\tau)}\right]V(\tau)d\tau}{m_{melt}\left[c_p\left(T_{melt} - T_{coolant}\right) + h_{fus}\right]} \tag{16}$$

In most of tests, tin drop with a mass ranged from 0.5~1.0 g at the melt temperatures up to 1200 ^oC dropped into subcooled water. If the melt diameter of 3 mm at the melt temperature of 1100 ^oC and the coolant temperature of 30 ^oC are taken in the one of tests, the maximum internal vapor pressure was estimated up to 30 MPa and the conversion ratio reached the maximum of approximately 0.5%. This value is consistent with many previous research works. More comprehensive analysis of the existing MISTEE data will be continued

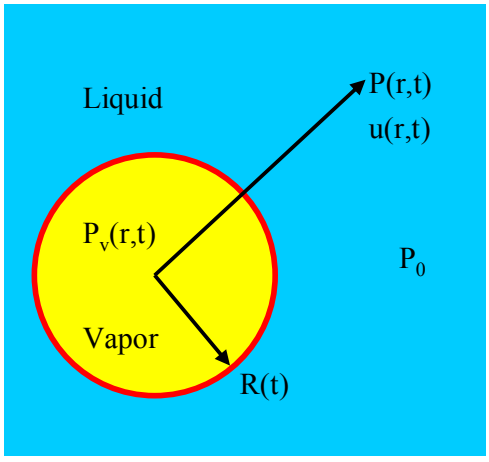

Figure 37: Schematic of a vapor bubble dynamics.

4.4 Oxidic Melt Tests

At present various binary oxidic melt as listed in Table 4 has been tested to develop the techniques to generate and deliver a single drop melt for the MISTEE experiments. The binary oxide, $CaO-B_2O_3$, has high viscosity compared to corium and exhibits the characteristics of glass-type oxides. It has relatively low melting point. The other oxides such as Al_2O_3, WO_3-CaO and $MnO-TiO_2$ have the characteristic of ceramic type of oxides similar to the corium. However, the melting temperatures of these oxides except the WO_3-CaO are much higher.

Table 4: Thermo-physical properties of single and binary oxidic melts for the MISTEE experiments comparing to Corium and Tin

	Corium ($80UO_2$-ZrO_2)	Sn	Al_2O_3	$CaO-B_2O_3$ (30-70)	WO_3-CaO (82-18)	$MnO-TiO_2$ (78-22)
T_{ref} (^oC)	2600	1000	2800	1100	1200	1400
ρ (kg/m^3)	7320 (liq.)	6507	2027	2500 (liq.)	6500 (sol.)	4500
T_{mp} (^oC)	2600 (liq.) 2500 (sol.)	232	2500	1030 (liq.) 980 (sol.)	1200 (liq.) 1135(sol.)	1380 (liq.)
C_p (kJ/kgK)	0.54 (liq.) 0.41 (sol.)	0.26	1.4	2.20 (liq.) 1.53 (sol.)	0.5	0.9
h_{fus} (kJ/kg)	360	59.5	1000	460	70	-
k (W/mK)	9.6 (liq.)	32	8	3.0 (liq.) 2.1 (sol.)	-	-
μ (mPa/s)	3.7	0.87	4	100~300	-	-
σ (N/m)	1.02	0.53	0.5	0.15	-	-

Recently, a $MnO-TiO_2$ melt at the initial temperature of approximately 1400 ^oC was successfully prepared and delivered into water at 50 ^oC. The $MnO-TiO_2$ melt drop at eutectic pint shown in Table 4 was placed in the boron nitride coated Alumina crucible which again inserted the graphite block in the MISTEE induction furnace. The $MnO-TiO_2$ is melted by the in-direct heating of graphite block. The melt temperature was monitored by C-type thermocouple. The entire melt generating unite was placed in an inert atmosphere provided by purging Argon gas during the melting process to protect the C-type thermocouple. The melt drop release mechanism was the same as the one used in the tin tests. All experimental procedures, thereby, are the same. These scoping tests used newly developed the simultaneous high-speed visualization system with X-ray radiography and photography by adding one more high-speed camera (see details in the next section). Figure 38a showed the photographic image of the $MnO-TiO_2$ melt drop which was deformed during the penetration into water.

The Figure 38b showed the X-ray radiographic image of the same $MnO-TiO_2$ drop as shown in Figure 36a that the droplet has an internal cavity. Both images revealed the deformation of the originally round melt drop to a drop with large center cavity

created by a shear force exerted to the melt surface during falling. The melt surface is still hot (red in Figure 38a) and the cavity has a chance to entrap surrounding water which triggers the energetic FCIs. There was a small explosion. However, since the melt superheat was not sufficient to maintain the liquid phase of the melt, major FCI was not initiated. This effort continues.

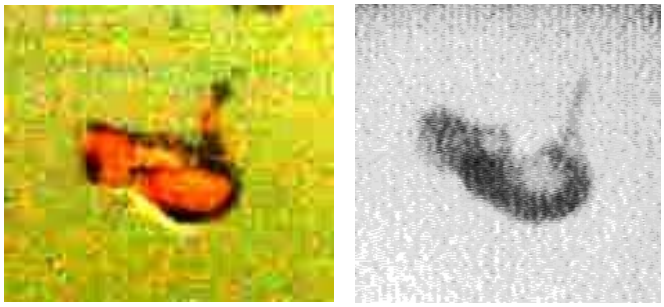

(a) (b)

Figure 38: MnO-TiO_2 melt drop (~1400 ^oC) into water: (a) photography image and (b) X-ray radiography image.

4.5 Development of Simultaneous Visualization System

One significant improvement of our X-ray radiography system in the MISTEE facility has been achieved by adding additional high-speed CMOS camera (Redlake HG50LE Color CMOS Camera, 100,000 fps maximum). This improvement provides the simultaneous synchronized visualization using two high-speed cameras, one for X-ray radiography and another for photography, called SHARP (**S**imultaneous **H**igh-Speed Visual **A**cquisition with X-ray **R**adiography and **P**hotography) (see Figure 39) where synchronized visual data for vapor bubble and melt fragment dynamics, will enable the accurate quantification of the steam explosions.

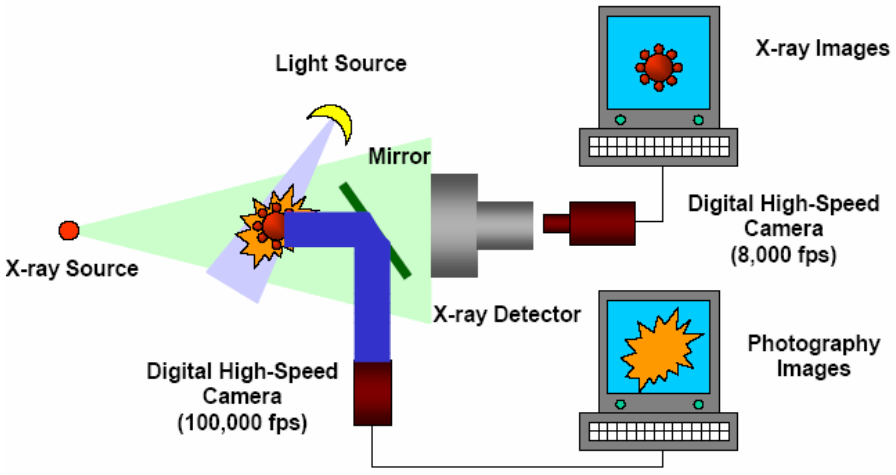

Figure 39: The schematic of the SHARP system.

One high-speed camera (photography) visualizes the dynamic behavior of vapor film surrounding a melt drop during the vapor explosion process. This information will provide data on the interaction zone of steam-melt-water mixture as well as the transient steam bubble dynamics. The data on interaction zone will be used to

quantify the volume fractions of each component involved in vapor explosion derived from the image data from the X-ray radiography. The data on the transient bubble dynamics in combination with dynamic pressure signals will be used to estimate the energetics or explosivity, of the vapor explosion, in terms of explosion conversion ratio (the ratio of work done by the explosion process on the environment to the total initial energy content of the melt droplet).

The other camera (X-ray radiography) visualizes the melt fragmentation process during the explosion phase of vapor explosion. This image data will provide the visual information on the fine fragmentation and triggering processes and eventually be quantified after a series of calibration tests. This transient fragmentation data will be used to evaluate the current-existing analytical fragmentation models and to propose a new model if necessary. In addition, the X-ray image data will provide the characteristic and location of initial triggering and small-scale propagation processes. Dynamic behavior of finely fragmented melt particles will be also important data to evaluate the existing analytical explosion models which employ local heat transfer among the fine particles, un-fragmented melt, vapor and water in the interaction zone.

Image processing is one of important tasks because the quantification of the fine fragmentation of a melt-drop during the vapor explosion is based on the images taken by both photography and X-ray radiography. In particular, the X-ray images have significant amount of background image noise because of the X-ray back scattering and inefficiency of scintillation detector and phosphor screen. In addition to this, to quantify the data, a series of calibration tests with known geometry and material contents have to be performed.

This system will be the main visualization system to be used in the coming investigation of the MISTEE program.

Chapter 5
Summary and Conclusions

The ExCoolse project aimed to investigate the some of key unresolved severe accident issues such as coolability of particulate porous debris bed and melt pool and energetic fuel-coolant interactions. The following is the summary and conclusions of the work.

5.1 Melt Debris Bed Coolability (POMECO Program)

The enhancement of coolability of porous corium outside of the reactor vessel due to incorporation of downcomers for both the particulate debris beds in the multi-dimensional aspects is investigated. In this project, the previous POMECO facility had been successfully modified to investigate the coolability of radially stratified particulate debris beds. No radially-stratified bed experiments and multiple water injection were performed in the previous POMECO facility, although axially-stratified beds were constructed and their characteristics measured.

The purpose of the modified POMECO facility is to (a) add more downcomers in the debris bed to determine the interaction (b) add radial stratification of particulate debris beds and (c) add side injection line to determine multi-dimensional effects in coolability.

The following main observations resulted from this study:

- The quenching rate with top flooding alone is very small and with non-condensable gases during MCCI, CCFL conditions may exist and it may not be possible to quench the bed.

- Water injection at the periphery of the bed reduces the quenching period. However, bottom flooding using downcomers in addition to top flooding reduces the quenching period significantly. The quenching period is found to be affected by the location and size of the downcomers which bring water from the top over-layer water to the bottom of the bed.

- Quenching rate in the low porosity layer is always found to be lower than that in the high porosity layer.

- Non-condensable gases systematically delay the quenching rate both in low and high porosity layers. However, this effect was found to be larger in the higher porosity layer than in the lower porosity layer.

- The quenching behavior was almost similar with air and argon. However, the quenching period was found to be little longer with argon than with air for the same injection mass flow rate.

5.2 Melt Pool Coolability (COMECO Program)

Experiments were carried out in the COMECO facility to study the water ingression phenomena in melt pool and its coolability. The COMECO facility is employ one downcomer unit cell, while the modified POMECO can employ radially-stratified debris bed with multiple water injection and bottom flooding using downcomers, in order to observe any interaction effects.

Experiments were carried out with the melt prepared from the binary oxide mixture of CaO (30% by wt.) and B_2O_3 (70% by wt.) and $MnO+TiO_2$ melt. A number of attempts with $MnO+TiO_2$ melt were failed due to the high temperature of the melting point of the mixture and it is difficult to achieve with the existing furnace. The unexpected failure of the melt generator and heating system in the COMECO facility was occurred during the first experiment for the melt coolability with the very high-temperature binary oxidic melt, $78\%MnO+22\%TiO_2$ whose liquidus temperature is 1380 ^oC. The temperature of the crucible inside the induction furnace reached ~ 1500 ^oC which caused it structural failure. The capacitor and electric unit within the induction furnace overheated and failed. Two heaters in the COMECO facility also were failed during experiment and dismantling.

For this the $CaO+B_2O_3$ material was used to simulate the corium melt during the later phases of the accident progression. The water ingression phenomenon was studied for top flooding conditions. The preliminary results indicate that water could hardly ingress up to a depth of 7 to 8 cm beneath the top of the pool. Hence, it may not be possible to quench the melt pool by top flooding alone. The temperature history at different axial and radial positions was recorded.

Due to the major failure of the melt generator system, the experiment has not been resumed since the failure.

5.3 Energetic FCIs (MISTEE Program)

It has been clearly indicated that the conversion ratio (or energetic yield) in a triggered UO_2–ZrO_2 explosion is significantly less than that in a triggered Al_2O_3 or stainless steel melt explosion. There are some limiting mechanisms which reduce the yield for non-eutectic oxidic mixtures. Since it is infeasible to perform large-scale steam explosion experiments with UO_2–ZrO_2 or UO_2–ZrO_2–Zr and it is very difficult to establish a scaling relationship, more fundamental investigation is needed in terms of identifying the limiting mechanisms. We have constructed the micro interaction steam explosion experiments (MISTEE) facility, wherein, currently, we are observing the differences between the characteristics of the explosion phase of a steam explosion, for a single droplet, of different material (metal, single oxide, binary oxide mixture, binary oxide and metal mixture, etc.) melts.

The followings are the summary of the activities in the MISTEE facility:

- The metallic melt tests with molten tin droplet have been completed. The evaluation methodology of energetics of single drop FCIs was developed and preliminary analysis showed less than 0.5% conversion ratios were estimated.

The evaluation used the experimental data such as transient pressure signal and vapor bubble dynamics visualized by the high speed photography. X-ray radiographic images reveal the transient structure of FCIs at various thermal conditions.

- Evaluation of quantification methodology of X-ray radiography image for melt fraction during FCI has been performed and generated a transient melt fragmentation map.

- Simultaneously synchronized high-speed visualization with X-ray radiography and photography system was under development by adding a new ultra-fast CMOS high-speed camera at the maximum frame rates of 100,000 fps.

- Melt generation and delivery techniques for various oxidic melt drops have been tested and developed. Glass type viscous melts such as $CaO\text{-}B_2O_3$ never showed energetic FCI events. However, preliminary tests with $MnO+TiO_2$ partially triggered. In this test for the first time, the SHARP visualization techniques was used and revealed the necessity of such a technique for the high temperature FCIs, in which visual observation of the structure of melt during FCIs was largely hindered by the vapor and bright radiant from the high-temperature melt surface.

Some of findings fro the metallic tin tests are as follows:

- The relatively small portion of a single drop melt was always pre-fragmented by the first perturbation mostly induced by the external shock wave. The major energetic FCI occurs when pre-fragmented drops were triggered.

- The oscillation of vapor bubble during expansion and collapse continuously induces the energetic FCIs and generate finely fragmented melt debris.

- For highly subcooled water, the small-scale stratified explosion initiated at the circumference or lower hemispherical region of an ellipsoidal or spherical droplet, respectively and propagated along the melt surface.

- For lower subcooled water, the vapor/gas pocket formed during the impingement of molten tin drop into water and film boiling heat transfer in water provide an extra triggering source. The maximum expansion diameter of fragmented particles and vapor bubble reached 3~3.5 times the initial diameters.

- X-ray radiographic images showed a shell of fragmented melt particle near the vapor bubble boundary during the explosions. Transient spatial distribution map of melt fragment during the explosion was obtained. However, further improvement in X-ray image is still required for accurate quantitative measurement.

In this study, the work will continue to identify the mechanisms of energetic FCIs in terms of material differences and thermal conditions by using the MISTEE facility with the SHARP technique.

References

1 Akiyoshi, R., Nishio, S., and Tanasawa, I., 1990, "A Study on the Effect of Non-condensable Gas in the Vapor Film on Vapor Explosion," Int. J. Heat Mass Transfer, **33** (4), pp. 603~609.

2 Alsmeyer, H., Spencer, B., Tromm, W., 1998. The COMET-concept for cooling of ex-vessel corium melts, Proc. of ICONE-6, May 10–15, San Diego.

3 Blose, R.E., Gronager, J.E., Suo-Anttila, A.J., and Brockmann, J.E. 1987. SWISS: Sustained heated metallic melt-concrete interactions with overlaying water pools. NUREG/CR-4727, SAND85-1546 R3, R4, R7.

4 Blose, R.E., Powers, D.A., Copus, E.R., Brockmann, J.E., Simpson, R.B., and Lucero, D.A. 1993. Core-concrete water interactions with overlaying water pools – the WETCOR 1 test. NUREG/CR-5907.

5 Broughton, J.M. et al., 1989. A Scenario of the Three Mile Island Unit 2 Accident. Nucl. Tech. 87 1, pp. 34–53.

6 Catton, I., Dhir, V. and Somerton, C. 1983. An Experimental Study of Debris Coolability under Pool Boiling Conditions. *Technical Report NP-3094*, EPRI.

7 Cho, D.H., and Bova, L. 1983. Formation of dry pockets during water penetration into a hot particle bed. *Trans. ANS* **, 41**, 418.

8 Ciccarelli, G., 1991, Investigation of Vapor Explosions with Single Molten Metal Drops in Water Using Flash X-ray, Ph.D. Thesis, McGill University, Canada.

9 Dhir, V. and Catton, I. 1977. Study of Dryout Heat Fluxes in Beds of Inductively Heated Particles. *Technical Report CR-0262*, NUREG.

10 Farmer, M.T., Aeschlimann, R.W., Kilsdonk, D.J., and Spencer, B.W. 2000. Results of MACE Test M3b posttest debris characterization. ACEX-TR-31.

11 Farmer, M.T., and Spencer, B.W. 2001. A review of database pertaining to ex-vessel debris coolability. ACEX-TR-C34.

12 Farmer, M.T., Sienicki, J.J., and Kovtonyuk, A. 2003. OECD MCCI analytical support (stand alone task) water ingression modelling of the OECD/MCCI SSWICS tests. NRC/MCCI/2003-TR01.

13 Farmer, M.T., Lomperski, S., and Basu, S. 2004. Results of reactor material experiments investigating 2-D core-concrete interaction and debris coolability. *Proceedings of ICAPP-04*, June 13-17, Pittsburg, USA.

14 Hardee, H. and Nilson, R. 1977. Natural Convection in Porous Media with Heat Generation. *Nuclear Science and Engineering*, **63**, 119-132.

15 Hu, K. and Theofanous, T.G. 1984. Scale Effects and Structure of Dryout Zone in Debris Bed Coolability. *Proceedings of 6th Information Exchange Meeting on Debris Coolability,* UCLA, USA.

16 Huhtiniemi, I. and Magallon, D. 1999. Insight into steam explosion with corium metals in KROTOS. *NURETH-9*, October 3-8, USA.

17 Jasiulevicius, A., Sehgal, B.R. 2003. Debris Bed Quenching with Non-condensable gas Addition from Bottom, *ICONE-11*, April 20-23.

18 Konovalikhin, M.J., Jasiulevicius, A., Sehgal, B.R., "Debris bed coolability in the BWR pressure vessel", Proceedings of 6th ASME-JSME Thermal Engineering Joint Conference, Kohala Coast, Havaii, USA, March 16-20, 2003.

19 Lindau, O., and Lauterborn, W., 2001, "Investigation of the Counterjet Developed in a Cavitation Bubble That Collapses Near a Rigid Boundary," Fourth International Symposium on Cavitation, Pasadena, USA, June.

20 Magallon, D., Hohmann, H. 1995. High pressure corium melt quenching tests in FARO. *Nucl. Eng. Des*., 155, 253-270.

21 Magallon, D. et al., 1999. Corium melt quenching tests at low pressure and subcooled water in FARO. Proc. NURETH-9.

22 Magallon, D., Basu, S. and Corradini, M. 1999. Implications of FARO and KROTOS experiments for FCI issues. *OECD Workshop on Ex-vessel Debris Coolability*. November, 15-18, Germany.

23 Merilo, M., Farmer, M.T., and Spencer, B.W. 1997. Status report on the MACE M3B experiment. *Proc. of CSARP meeting*, Behesda, Maryland.

24 Nagasaka, H., Sakaki, I., Kato, M., Vasilyev, Y., Kolodeshnikov, A. and Zhdanov, V. 1999. COTELS Project (3): Ex-vessel debris cooling tests. *OECD Workshop on Ex-vessel Debris Coolability*. November, 15-18, Germany.

25 Nelson, L.S., and Duda, P.M., 1981, "Steam Explosion Experiments with Single Drops of Iron Oxide Melted with a CO_2 Laser," NUREG/CR-2295, NRC, USA.

26 Pilch, M., and Erdman C.A., 1987, "Use of Breakup Time Data and Velocity History Data To Predict The Maximum Size of Stable Fragments for Acceleration Induced Breakup of a Liquid Drop," Int. J. Multiphase Flow, **13**, No. 6, pp. 741~757.

27 Reed, A., Boldt, K., Gorham-Bergeron, R., Lipinski, R. and Schmidt, T. 1985. Dcc-1 and Dcc-2 degraded Core Coolability Analysis, *Technical Report CR-439*, SAND85-1967, NUREG.

28 Schrock, V.E., Wang, C.H., Revankar, S., Wei, L.H., Lee, S.Y., Squarer, D. 1984. Flooding in Particulate Beds and their Role in Dryout Heat Flux, *Proceedings of 6th Information Exchange Meeting on Debris Coolability,* UCLA, USA.

29 Sehgal, B.R. et al., 1992. MACE project overview. Proceedings of the OECD Meeting on Core Debris Concrete Interaction, Karlsruhe Germany.

30 Sehgal, B.R., and Spencer, B.W. 1992. Ace Program Phase D: Melt attack and coolability experiments (MACE) Program. *2nd Specialist Meeting on Molten Core Debris – Concrete Interactions,* Karlsruhe, Germany.

31 Sehgal, B.R., Konovalikhin, M.J., Yang, Z.L., Kazachkov, I.V., Amjad, M., Li, G.J. 2001. Experimental Investigations on Porous Media Colability, *RIT/NPS Research report*.

32 Sehgal, B.R. and Park, H.S. 2004, Assessment of Severe Accident Management Issues in the Nordic BWRs and PWRs, Final Report of the PRE-DELI-MELT project, Contract No: AFT/NKS-R(02)9, NKS.

33 SERG2, 1995. SERG2 A reassessment of the potential for an Alpha-Mode containment failure and a review of the current understanding of broader fuel-coolant interaction (FCI) issues. NUREG-1529.

34 Spencer, B.W., Wang, K., Blomquist, C.A., McUmber, L.M., Schneider, J.P. 1994. Fragmentation and quench behaviour of corium melt streams in water. *NUREG/CR-6133*, Washington D.C., USA.

35 Theofanous, T.G. et al., An assessment of steam-explosion-induced containment failure. Nuclear Science and Engineering 97 (1987), pp. 259–326 Parts I-IV

36 Theofanous, T.G., Liu, C., and Yuen, W.W. 1998. Coolability and quench of corium-concrete interactions by top flooding. MACE-TR-D15.

37 Tung, V.X., Dhir, V.K., Squarrer, D. 1986. Quenching by Top Flooding of a Heat Generating Particulate Bed with gas Injection at the Bottom. *Proceedings of 6th Information Exchange Meeting on Debris Coolability*, EPRI Report NP-4455.

38 Tung, V.X. and Dhir, V.K. 1987. Quenching of Debris Beds having Variable Permeability in the Axial and Radial Directions. *Nuclear Engineering and Design*, 99, 275-284.

Bibliographic Data Sheet **NKS-112**

Title	Ex-Vessel Coolability and Energetics of Steam Explosions in Nordic Light Water Reactors - EXCOOLSE Project Report 2004
Author(s)	H. S. Park, A. K. Nayak, R. C. Hansson & B. R. Sehgal
Affiliation(s)	Royal Institute of Technology, Division of Nuclear Power Safety, Sweden
ISBN	87-7893-173-8 *(Electronic report)*
Date	October 2005
Project	NKS_R_2004_36
No. of pages	56
No. of tables	4
No. of illustrations	39
No. of references	38
Abstract	Beyond-the-design-basis accidents, i.e. severe accidents, involve melting of the nuclear reactor core and release of radioactivity. Intensive research has been performed for years to evaluate the consequence of the postulated severe accidents. Severe accidents posed, to the reactor researchers, a most interesting and most difficult set of phenomena to understand, and to predict the consequences, for the various scenarios that could be contemplated. The complexity of the interactions, occurring at such high temperatures (~2500ºC), between different materials, which are changing phases and undergoing chemical reactions, is simply indescribable with the accuracy that one may desire. Thus, it is a wise approach to pursue research on SA phenomena until the remaining uncertainty in the predicted consequence, or the residual risk, can be tolerated. In the PRE-DELI-MELT project (Sehgal and Park, 2004) at NKS, several critical issues on the core melt loadings in the BWR and PWR reactor containments were identified. Many of Nordic nuclear power plants, particularly in boiling water reactors, adopted the Severe Accident Management Strategy (SAMS) which employed the deep subcooled water pool in lower dry-well. The success of this SAMS largely depends on the issues of steam explosions and formation of debris bed and its coolability. From the suggestions of the PRE-DELI-MELT project, a series of research plan was proposed to investigate the remaining issues specifically on the ex-vessel coolability of corium during severe accidents; (a) ex-vessel coolability of the melt or particulate debris, and (b) energetics and debris characteristics of fuel-coolant interactions endangering the integrity of the reactor containments.
Key words	Severe accidents, melt coolability, ex-vessel, debris characteristics

Available on request from the NKS Secretariat, P.O.Box 49, DK-4000 Roskilde, Denmark.
Phone (+45) 4677 4045, fax (+45) 4677 4046, e-mail nks@nks.org, www.nks.org